

Journal of Materials Chemistry C

Materials for optical, magnetic and electronic devices

Accepted Manuscript

This article can be cited before page numbers have been issued, to do this please use: J. Yang, Y. Liu, W. Yan, P. Zhou, Z. Wang, Y. Wang, Y. Zhang, Z. Zhang, F. Mo, Z. Ji, H. Haick and Y. Wang, *J. Mater. Chem. C*, 2025, DOI: 10.1039/D5TC01896J.



This is an Accepted Manuscript, which has been through the Royal Society of Chemistry peer review process and has been accepted for publication.

Accepted Manuscripts are published online shortly after acceptance, before technical editing, formatting and proof reading. Using this free service, authors can make their results available to the community, in citable form, before we publish the edited article. We will replace this Accepted Manuscript with the edited and formatted Advance Article as soon as it is available.

You can find more information about Accepted Manuscripts in the [Information for Authors](#).

Please note that technical editing may introduce minor changes to the text and/or graphics, which may alter content. The journal's standard [Terms & Conditions](#) and the [Ethical guidelines](#) still apply. In no event shall the Royal Society of Chemistry be held responsible for any errors or omissions in this Accepted Manuscript or any consequences arising from the use of any information it contains.

Open Access Article. Published on 05 srpna 2025. Downloaded on 20.08.2025 13:06:50.
This article is licensed under a Creative Commons Attribution-NonCommercial 3.0 Unported Licence.



1 **Conductive Hydrogel-based Epidermal Electrodes for Electrophysiological**
2 **Monitoring**

3 *Jiawei Yang^{a,b}, Yi Liu^{a,b}, Wenqing Yan^{a,b}, Pengcheng Zhou^{a,b}, Zonglei Wang^{a,b}, Yuli*
4 *Wang^{a,b}, Yujie Zhang^{a,b}, Zongman Zhang^{a,b}, Fan Mo^c, Zichong Ji^{a,b}, Hossam Haick^b,*
5 *Yan Wang^{a,b,d}**

6
7 ^a Department of Chemical Engineering, Guangdong Technion-Israel Institute of
8 Technology 241 Daxue Road, Shantou, Guangdong 515063, China

9 ^b The Wolfson Department of Chemical Engineering, Technion-Israel Institute of
10 Technology, Haifa 3200003, Israel

11 ^c Department of Materials Science and Engineering, Technion-Israel Institute of
12 Technology, Haifa 3200003, Israelpp

13 ^d Guangdong Provincial Key Laboratory of Materials and Technologies for Energy
14 Conversion, Guangdong Technion-Israel Institute of Technology, 241 Daxue Road,
15 Shantou, Guangdong 515063, China

16
17 **Keywords:** Conductive hydrogels; epidermal electrodes; electrophysiological
18 monitoring

19
20 ***E-mail:** wang.yan@technion.ac.il; yan.wang@gtiit.edu.cn

Abstract

Electrophysiological signals generated by human physiological processes offer critical insights for health monitoring and disease diagnosis, with their precise acquisition depending on high-performance electrodes. Conductive hydrogel-based epidermal electrodes, owing to their superior properties, demonstrate significant promise in electrophysiological monitoring. This review presents a comprehensive summary of the recent progress in the design and application of conductive hydrogels for epidermal electrophysiological electrodes. It first categorizes the various types of conductive hydrogel materials, highlighting recent advancements and their unique advantages as electrode interfaces. Subsequently, the key properties of conductive hydrogel-based epidermal electrodes are discussed, including conductivity, adhesion, stretchability, and gas-permeability. Then, state-of-the-art applications across multiple electrophysiological domains are introduced, ranging from electrocardiography, electromyography, electrooculogram, and electroencephalography. Finally, a conclusion and future directions for the conductive hydrogel-based epidermal electrodes in electrophysiological monitoring are provided.



1. Introduction

Electrophysiological signals, including electrocardiogram (ECG), electromyogram (EMG), electroencephalogram (EEG), and electrooculogram (EOG), reflect critical human physiological processes, capturing bioelectric activity from heartbeats, muscle contractions, and neural functions¹. These signals are essential for diagnosing and monitoring cardiovascular conditions^{2, 3}, investigating neurological disorders^{4, 5}, supporting motor rehabilitation^{6, 7}, and advancing human-computer interaction systems^{8, 9}. Characterized by high temporal and spatial complexity, these signals exhibit amplitudes ranging from microvolts to millivolts and frequencies spanning sub-hertz to hundreds of hertz¹⁰. Consequently, skin-mountable electrodes, as the cornerstone of electrophysiological signal acquisition, must combine high sensitivity, mechanical stability, stretchability, and conformal skin contact to maintain signal fidelity and improve clinical outcomes¹¹⁻¹⁵.

Electrodes are generally categorized as invasive or non-invasive and serve as critical interfaces in biochemical sensing and human health monitoring, enabling efficient transmission and transduction between biological signals and electronic systems¹⁶⁻²⁰.

Invasive electrodes, implanted to directly interface with target tissues, yield high-resolution signals but are constrained by surgical risks and invasiveness, limiting their use in routine monitoring. Non-invasive electrodes, which capture signals through skin contact, are further divided into dry and wet electrodes. Dry electrodes, typically constructed from metals or rigid conductive materials, are valued for their reusability and ease of application but exhibit high stiffness, making it challenging to maintain intimate skin contact during dynamic deformation or movement²¹. This often results in skin-electrode contact gaps, elevating interface impedance and diminishing the signal-to-noise ratio (SNR). Wet electrodes, such as commercial Ag/AgCl gel electrodes, utilize conductive gel to enhance skin-electrode contact for lower skin-electrode impedance, delivering high-quality signals in the short term²². However, they typically



64 rely on semi-liquid conductive gels, prolonged use may lead to discomfort, allergic
65 reactions, or signal attenuation due to gel desiccation or skin irritation. Moreover, their
66 rigidity hampers signal acquisition in dynamic settings. In recent years, advancements
67 in flexible electronics have positioned epidermal electrodes made from flexible
68 materials as compelling alternatives to conventional electrodes²³⁻²⁵. With exceptional
69 stretchability (exceeding 200% strain), skin-matched low modulus, and ultra-thin
70 profiles, these electrodes establish soft, stable skin interfaces, markedly reducing skin
71 contact impedance and enhancing SNR. Consequently, the development of flexible
72 epidermal electrodes optimized for long-term, stable signal acquisition has emerged as
73 a pivotal research priority.

74 Hydrogels are hydrophilic, cross-linked polymer networks that stably retain at least 10
75 wt % water within their three-dimensional structure²⁶. This structure imparts
76 exceptional biocompatibility and a low Young's modulus, rendering hydrogels ideal
77 for skin-contact applications^{27, 28}. Traditional hydrogels generally exhibit poor
78 electrical conductivity, which impairs their ability to respond to external signals and
79 restricts their effectiveness in electrophysiological signal acquisition. To address this,
80 researchers have engineered conductive hydrogels by integrating conductive
81 elements—such as conductive polymers, nanomaterials, or ions—achieving
82 remarkable electrical performance²⁹⁻³⁵. Fine-tuning the proportions of these
83 components enables precise control over hydrogel conductivity. Furthermore, through
84 innovative structural and chemical designs, conductive hydrogels can exhibit superior
85 mechanical toughness, high conductivity, self-adhesion, and breathability^{36, 37}.

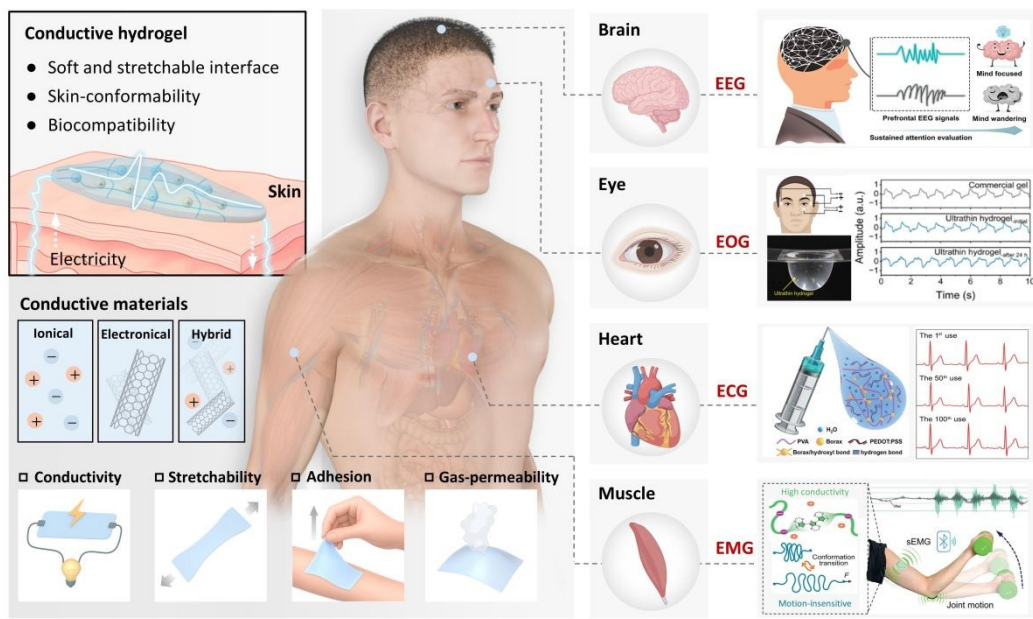
86 In recent years, conductive hydrogels have attracted significant research interest due to
87 their promising applications in bioelectronics and wearable devices³⁸⁻⁴⁰. For example,
88 Mo et al.⁴¹ reviewed recent advancements in ionic conductive hydrogels for skin sensor
89 applications. While previous reviews have focused on specific subtypes—such as ionic
90 liquid (IL)-based or nanomaterial-based conductive hydrogels—there remains a lack of
91 comprehensive discussion on their role as epidermal electrodes for electrophysiological



Open Access Article. Published on 05 srpna 2025. Downloaded on 20.08.2025 13:06:50.
This article is licensed under a Creative Commons Attribution-NonCommercial 3.0 Unported Licence.



92 monitoring^{25, 42-44}. Ding et al.⁴⁵ summarized the progress of conductive hydrogels in
93 electrophysiological signal acquisition; however, a holistic review encompassing
94 material design, performance requirements, and practical applications in
95 electrophysiological monitoring is still lacking. Therefore, this review aims to provide
96 a comprehensive overview of the latest research trends in conductive hydrogel-based
97 epidermal electrodes for electrophysiological applications. We begin by systematically
98 introducing the typical materials used in conductive hydrogels, including design
99 strategies for electronically conductive, ionically conductive, and hybrid conductive
100 systems. Next, we discuss the key performance requirements for conductive hydrogel
101 epidermal electrodes, such as conductivity, adhesion, stretchability, and gas-
102 permeability. Finally, we summarize recent advances in their application for monitoring
103 various electrophysiological signals (Fig. 1).



104
105 **Fig. 1 Schematic interpretation of conductive hydrogel-based epidermal**
106 **electrodes for electrophysiological monitoring.** The left side illustrates representative
107 types of conductive hydrogel materials, including ionic-based, electronic-based, and
108 hybrid-based, along with their key properties, such as electrical conductivity,
109 stretchability, adhesion, and gas permeability. The right side exhibits representative
110 examples of electrophysiology monitoring, including ECG, EMG, EEG, and EOG.
111 Reproduced with permission [46,47]. Copyright 2023, 2025, Wiley-VCH. Reproduced
112 with permission [48]. Copyright 2024, Springer Nature. Reproduced with permission
113 [49]. Copyright 2024, American Association for the Advancement of Science.

2. Materials of Conductive Hydrogel-based Epidermal Electrodes

Conductive hydrogels are composed of selectively introduced conductive fillers embedded in a cross-linked hydrophilic polymer matrix. Based on this fabrication method and configuration, we divide the epidermal electrodes based on conductive hydrogels into three categories: ionically conductive materials, electronically conductive materials, and hybrid conductive systems. In this section, we will discuss the representative materials of these three conductive hydrogel-based epidermal electrodes.

2.1 Ionically conductive hydrogel-based epidermal electrodes

Hydrogels, composed of one or more hydrophilic polymers, can absorb and retain significant amounts of water within their three-dimensional network structure⁵⁰. Leveraging the intrinsic hydrophilicity of hydrogel networks and the high mobility of ions in aqueous environments, ionically conductive hydrogels are typically formed by incorporating mobile ions into a crosslinked, water-rich polymer matrix. These hydrogels conduct electricity through the transport of ions such as Na^+ , K^+ , and Cl^- within the hydrated phase, which serves as the primary conduction medium. Under an applied electric field, the ions migrate through the network, enabling efficient ionic conduction⁵¹. Ion-conductive hydrogels are classified into three typical conductive mechanisms according to the migration mode of charge carriers and the characteristics of the conductive path: electrolyte-based, polyelectrolyte-based, and IL-based⁵². In electrolyte-based hydrogels, ionic conductivity results from the migration of small, dissociated ions (e.g., Na^+ , Cl^-) through the water-rich polymer network. These ions—introduced by dissolving inorganic salts or acids—can migrate freely within the hydrated phase when an electric field is applied. Electrolyte-based hydrogels are typically formulated by embedding these electrolytes into the polymer matrix, with commonly used examples including sodium chloride (NaCl), potassium chloride (KCl),



140 lithium chloride (LiCl), sodium sulfate (Na_2SO_4), potassium dihydrogen phosphate
141 (KH_2PO_4), tetramethylammonium chloride (TMACl), lactic acid, and various citrate
142 salts⁴¹.

143 Among typical chlorides, LiCl as a dopant can impart high conductivity to hydrogels,
144 which significantly reduces skin contact impedance and enables the acquisition of high-
145 quality biopotential signals. Meanwhile, the introduction of ions can enhance the water
146 retention of hydrogels, which is crucial for achieving long-term stable monitoring of
147 biopotential signals⁵³. A typical example is that Li et al.⁵⁴ designed a body temperature-
148 triggered adhesive ionic conductive hydrogel based on biocompatible polyacrylamide
149 (PAM), gelatin, LiCl, and sodium alginate (SA) (PGS hydrogel). Li^+ can freely shuttle
150 within the network structure of the PGS hydrogel, and the flow of these ions imparts
151 conductivity to the hydrogel (Fig. 2a). The conductivity of the PGS hydrogel
152 significantly increases with increasing LiCl content, rising from 0.28 ± 0.01 to $5.69 \pm$
153 0.20 S/m (Fig. 2b). Furthermore, the conductivity of the PGS hydrogel remains largely
154 stable under various stretching conditions (Fig. 2c). Even when the PGS hydrogel is
155 stretched by 20% strain, the brightness of a light-emitting diode connected to it remains
156 nearly unchanged. This demonstrates the stable conductivity of the PGS hydrogel in
157 complex environments, facilitating high-quality electrophysiological monitoring.

158 Polyelectrolytes serving as ionically conductive fillers bear covalently bound ionic
159 groups (e.g., $-\text{COO}^-$, $-\text{SO}_3^-$) along the polymer backbone. In polyelectrolyte-based
160 hydrogels, conductivity arises primarily from the migration of mobile counter-ions (e.g.,
161 Na^+ , K^+) via ion hopping and segmental motion within the hydrated network^{55, 56}. These
162 hydrogels offer good mechanical strength, especially in double-network structures, and
163 their conductivity can be tuned by adjusting polymer concentration, crosslinking
164 density, and counterion type, making them suitable for hydrated and physiological
165 conditions. Typical polyelectrolyte fillers in hydrogels include polyacrylic acid (PAA)
166 and its derivatives, chitosan, SA, etc⁵². Lu et al.⁵⁷ developed a double-network (DN)
167 polyelectrolyte hydrogel, integrating polymer chain entanglement, chemical



crosslinking, and multiple strong and weak intermolecular interactions. The hydrogel consists of a PAM network and a polyelectrolyte network composed of polyelectrolytes (poly(diallyldimethylammonium chloride) and poly(diallyldimethylammonium chloride) (Fig. 2d). The mechanical properties and adhesive strength of polyelectrolyte DN hydrogels can be customized by modulating the proportions of PAM, polyelectrolyte, and cosolvent. The optimal formulation yields a tensile modulus of 10.8 kPa, a tensile strain at break of 1000% strain, and an adhesive strength of 37.8 kPa. Furthermore, the stability of the crosslinked PAM network, combined with the unique properties of polyelectrolytes that induce phase separation, ensures the hydrogel's stability even in salt solutions while exhibiting solvent-tunable transparency (Fig. 2e). Owing to the presence of polyelectrolytes, the hydrogel exhibits excellent conductivity. This conductive hydrogel can be stretched up to 1100% strain before reaching its breaking point while maintaining stable conductivity even under high tensile strain (Fig. 2f).

IL-based hydrogels incorporate room-temperature ILs—such as 1-ethyl-3-methylimidazolium bis(trifluoromethanesulfonyl)imide (EMIM-TFSI)—either as co-solvents or as dispersed conductive media within the hydrogel network. Their ionic conductivity stems from the unrestricted movement of both organic cations and anions, which act as charge carriers. These hydrogels exhibit high and humidity-independent ionic conductivity, excellent electrochemical stability, and strong anti-freezing and anti-drying properties. They are particularly suitable for long-term use in harsh environments and maintain good flexibility and thermal stability^{58, 59}. By polymerizing IL monomers into PIL, the inherent properties of IL can be transferred to the polymer chain, thereby obtaining ionic conductive hydrogels with high conductivity. Zhao et al.⁶⁰ prepared an ionic gel through one-step photoinitiated polymerization of 2,2,2-trifluoroethyl acrylate and N-isopropylacrylamide (NIPAm) in the hydrophobic ILs 1-ethyl-3-methylimidazolium bis(trifluoromethylsulfonyl)imide ([EMIm][TFSI]) (Fig. 2g). The ionic gel demonstrates exceptional transparency (94.8%), underwater self-



196 healing capability (up to 96%), toughness (3.93 MJ/m^3), and

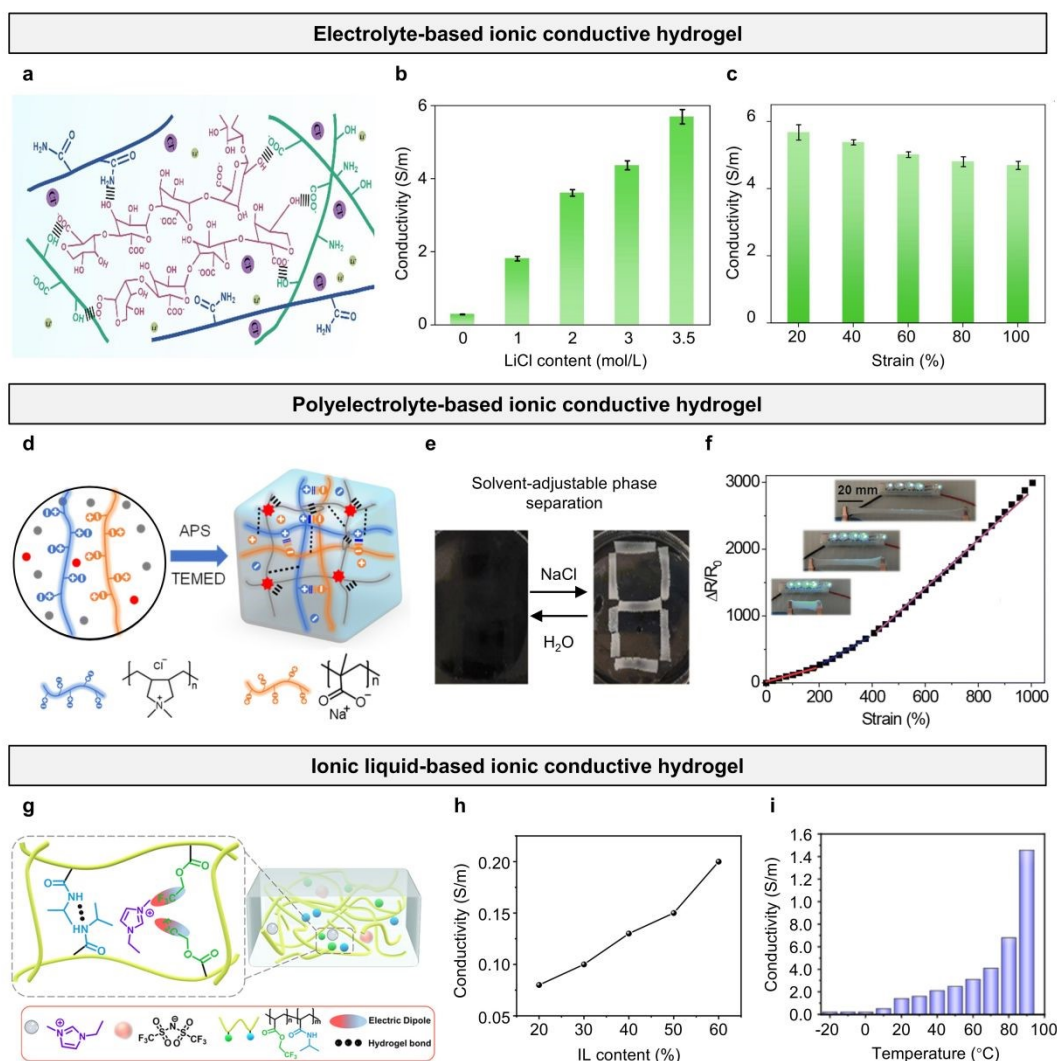


Fig. 2 Ionically conductive hydrogel-based epidermal electrodes. (a) PGS conductive hydrogel and its network structure. (b) Conductivity of PGS hydrogels with different LiCl contents. (c) Conductivity of PGS hydrogel under different strain. Reproduced with permission [54]. Copyright 2024, Elsevier. (d) Schematic diagram of the polyelectrolyte hydrogel preparation and structure. (e) The photograph illustrates the solvent-tunable transparency of the hydrogel electrolyte under induced phase separation. (f) Tensile strain induced relative resistance changes of the hydrogel. Reproduced with permission [57]. Copyright 2025, Royal Society of Chemistry. (g) Schematic diagram of the structure of the ionogel. (h) Conductivity of ionogel with different IL contents. (i) The ionic conductivities of the ionogel in the temperature range from -20 to 90°C . Reproduced with permission [60]. Copyright 2023, American Chemical Society.

underwater adhesion strength ($102.77 \pm 2.4 \text{ kPa}$). As the ILs mass percentage increased from 20% to 60%, the ionic gel's conductivity surged from 8.15×10^{-4} to 2.04×10^{-3}



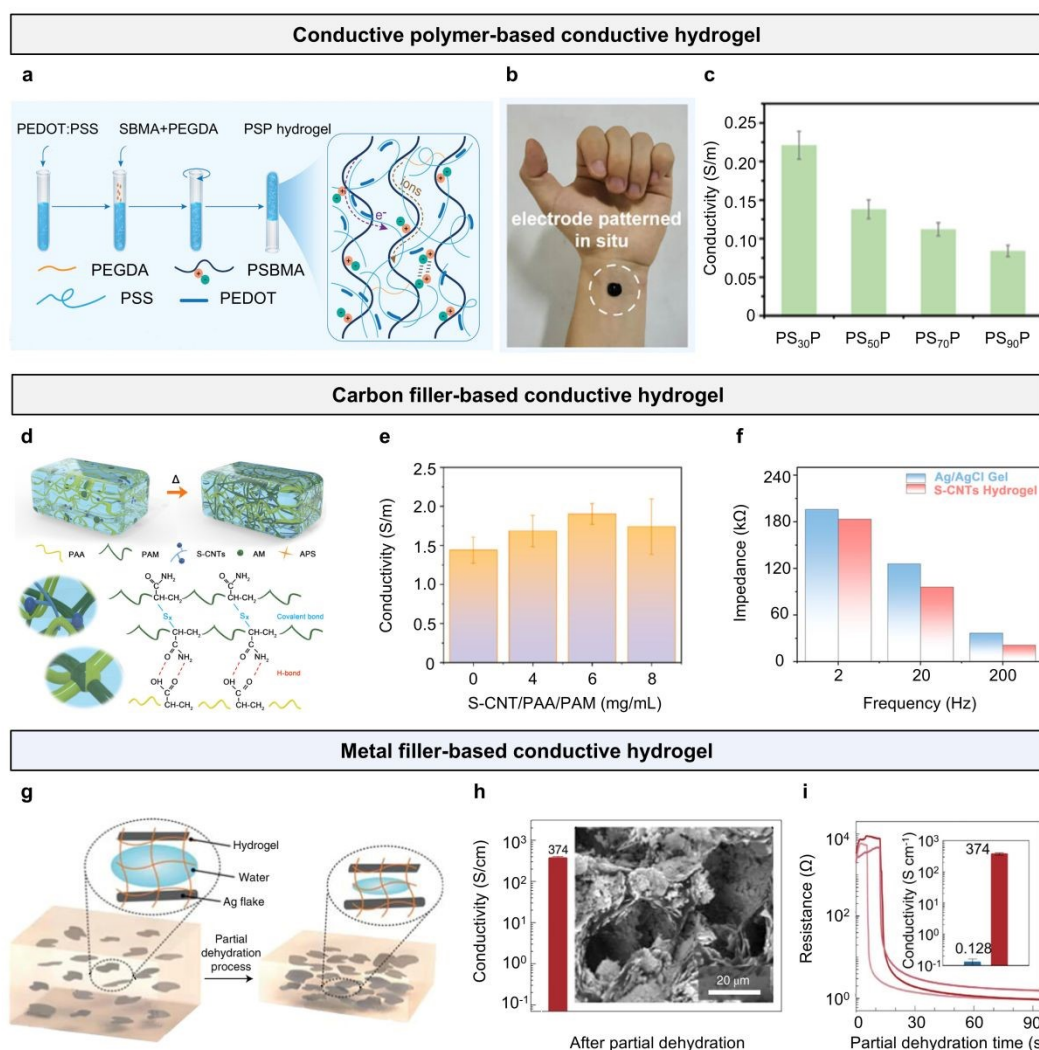
S/cm (Fig. 2h). Inspired by the excellent temperature responsiveness of IEs, the temperature sensitivity of the ionic gel was further characterized. Across a wide temperature range of -20 to 90 °C, the ionic gel exhibited high ionic conductivity (2×10^{-4} to 1.45×10^{-2} S/cm). Due to increased ion mobility, the ionic conductivity sharply increased with rising temperature (Fig. 2i).

2.2 Electronically conductive hydrogel-based epidermal electrodes

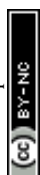
In electronically conductive hydrogel-based epidermal electrodes, the hydrogel matrix provides a soft, biocompatible scaffold, while embedded conductive materials enable efficient electron transport. Electrical conduction is achieved by incorporating intrinsically conductive components into the hydrogel network. These materials form continuous pathways that support charge transport through electron hopping or band-like conduction. The conductivity depends on factors such as filler dispersion and connectivity, polymer crystallinity, doping level, and interfacial interactions^{61, 62}. Electron conduction primarily encompasses three categories: i) conductive polymers, including poly(3,4-ethylenedioxythiophene) polystyrene sulfonate (PEDOT:PSS), polypyrrole (PPy), and polyaniline (PANi)^{63, 64}; ii) carbon filler-based nanomaterials, such as carbon nanotubes (CNTs) and graphene oxide (GO)^{65, 66}; and iii) metal-filler nanoparticles, such as silver nanoparticles (AgNPs)^{67, 68}. Incorporating these materials into hydrogels yields electron-conductive hydrogels with enhanced performance. A typical example is that Huang et al.⁶⁹ utilized PEDOT:PSS to promote the self-polymerization of zwitterionic [2-(methacryloyloxy)ethyl]dimethyl-(3-sulfopropyl) (SBMA), proposing an in-situ formed conductive hydrogel (PSP) (Fig. 3a). This hydrogel exhibits exceptional elasticity (elastic recovery rate $> 96\%$), robust adhesion strength (6.5 kPa), biocompatibility, and intrinsic antibacterial properties. The gelation process generates minimal heat (< 5 °C), enabling in-situ formation on the skin. Furthermore, the hydrogel achieves intimate skin contact, creating a highly conformal interface (Fig. 3b). The PSP hydrogel exhibits high conductivity, attributed to its



239 polycrystalline ionic network and conductive PEDOT:PSS. As the SBMA content
 240 increases, electronic conductivity of the PSP hydrogel decreases from 0.08 to 0.03 S/m,



241
 242 **Fig. 3 Electronically conductive hydrogel-based epidermal electrodes.** (a)
 243 Schematic diagram of the fabrication and promising applications of PSP hydrogel. (b)
 244 Photographs shows that the PSP hydrogel can be patterned on skin in situ. (c) The
 245 conductivity of the PSP hydrogel with different SBMA content. Reproduced with
 246 permission [69]. Copyright 2023, Wiley-VCH. (d) Schematic illustration of the
 247 preparation process of the S-CNTs/PAA/PAM hydrogel. (e) Conductivity of the
 248 prepared hydrogel with different S-CNTs content. (f) Impedance comparison at various
 249 frequencies of the S-CNTs/PAA/PAM hydrogel and commercial Ag/AgCl gel
 250 electrodes. Reproduced with permission [70]. Copyright 2025, American Chemical
 251 Society. (g) Composition of the conductive hydrogel composite composed of
 252 micrometre-scale Ag flakes and PAM-alginate hydrogel (Ag-hydrogel composite). (h)
 253 Conductivity of the Ag-hydrogel composite after the controlled partial dehydration
 254 process. (i) Conductivity of the Ag-hydrogel composite and micrographs of the
 255 composite after the controlled partial dehydration process. Reproduced with permission



[71]. Copyright 2021, Nature Publishing Group.

respectively. This reduction is attributed to the higher solid content and intensified inter- and intra-chain electrostatic interactions, which impede the formation of efficient conductive pathways. Nevertheless, the PSP hydrogel retains high conductivity, fully meeting the requirements for EMG monitoring (Fig. 3c).

Dai et al.⁷⁰ developed a hydrogel-based epidermal electrode composed of graphene nanoplates, PAA, and PAM (S-CNTs/PAA/PAM). S-CNTs, enriched with graphene nanoplates, are synthesized via a two-step sulphuration process employing thiourea and dibenzyl disulfide (Fig. 3d). The incorporation of sulfur atoms strengthens the interfacial interactions between S-CNTs and PAA/PAM through C–S covalent bonding, significantly improving the hydrogel's mechanical performance (> 1200% strain) and electrical conductivity (1.9 S/m). The incorporation of S-CNTs enhances the conductivity of PAA/PAM hydrogels to a certain extent. The 6S-CNTs/PAA/PAM hydrogel exhibits a conductivity of 1.9 S/m, surpassing that of the pristine PAA/PAM hydrogel (1.44 S/m). The unique chain structure of S-CNTs on the polymer chains shortens the charge migration pathway, thereby increasing the migration rate and improving conductivity. However, excessive addition of S-CNTs leads to their aggregation, which increases the overall resistance of the hydrogel and results in reduced conductivity (Fig. 3e). Moreover, the S-CNTs/PAA/PAM hydrogel, employed as an epidermal electrode for electrophysiological signal acquisition, demonstrates significantly lower skin-contact impedance than commercial Ag/AgCl gel electrodes across the 1–10⁵ Hz range (Fig. 3f).

Yunsik et al.⁷¹ designed a highly conductive, flexible hydrogel-based epidermal electrode by embedding micron-scale Ag particles within a PAM-alginate hydrogel matrix. A critical step in achieving high conductivity involves partial dehydration of the hydrogel matrix, facilitating the formation of percolation pathways by Ag flakes. Prior to partial dehydration, the Ag-hydrogel composite exhibits ionic conductivity with a low conductivity of ~0.13 S/cm. At this stage of the fabrication process, the volume fraction of Ag fillers (5 vol%) is insufficient to achieve percolation.



Subsequently, the conductivity of the composite increases significantly from 0.12 to 374 S/cm following dehydration (Fig. 3h). During the partial dehydration process, Ag-hydrogel composites with varying amounts of Ag added in-situ yielded the resistance values of the hydrogel. The resistance of the Ag-hydrogel composite decreased exponentially after drying for 10–15 minutes, stabilizing at $1.14 \pm 0.35 \Omega$ after 90 minutes, with a corresponding volume conductivity of 374 ± 30.8 S/cm (Fig. 3i).

2.3 Hybrid conductive hydrogel-based epidermal electrodes

Hybrid conductive hydrogels combine ionic and electronic conductive components within a single network, effectively addressing the limitations of pure systems. Ionically conductive hydrogels offer good biocompatibility and flexibility but often exhibit reduced conductivity under low humidity or freezing conditions. In contrast, electronically conductive hydrogels provide stable and high conductivity but may compromise stretchability and lack sufficient ionic transport. By integrating both mechanisms, hybrid hydrogels form synergistic, bicontinuous ion–electron conduction networks that enhance charge transport kinetics and conductivity stability. This dual-conduction design enables the hydrogel to maintain performance under mechanical deformation, temperature variation, and environmental stress. Additionally, hybrid networks allow tunable physical and electrical properties through molecular and structural engineering, such as tailoring polymer composition, conductive filler distribution, or crosslinking strategies⁷². For example, Luo et al.⁷³ designed an MXene-induced crosslinking fast-gelling hybrid conductive hydrogel electrode (PAAS) composed of acrylamide, NaCl, and MXene (Fig. 4a). Under the initiation of ammonium persulfate (APS), the C=C bonds of sodium acrylate are opened for polymerization, and then MXene acts as a crosslinker to rapidly form polymer chains. Meanwhile, the introduction of MXene increases the hydrogel's conductivity (2.3 S/m). In this system, sodium ions from NaCl and poly (sodium acrylate) impart ionic conductivity to hydrogel, while also establishing electrostatic interactions with MXene



and forming ionic coordination with acetic acid used for dissolving chitosan. Due to the addition of negatively charged MXene, the directional alignment of positively charged chitosan and sodium ions under an external electric field is restricted, reducing the hydrogel's polarization potential (change rate less than 6.5×10^{-4} V/min) (Fig. 4b and c).

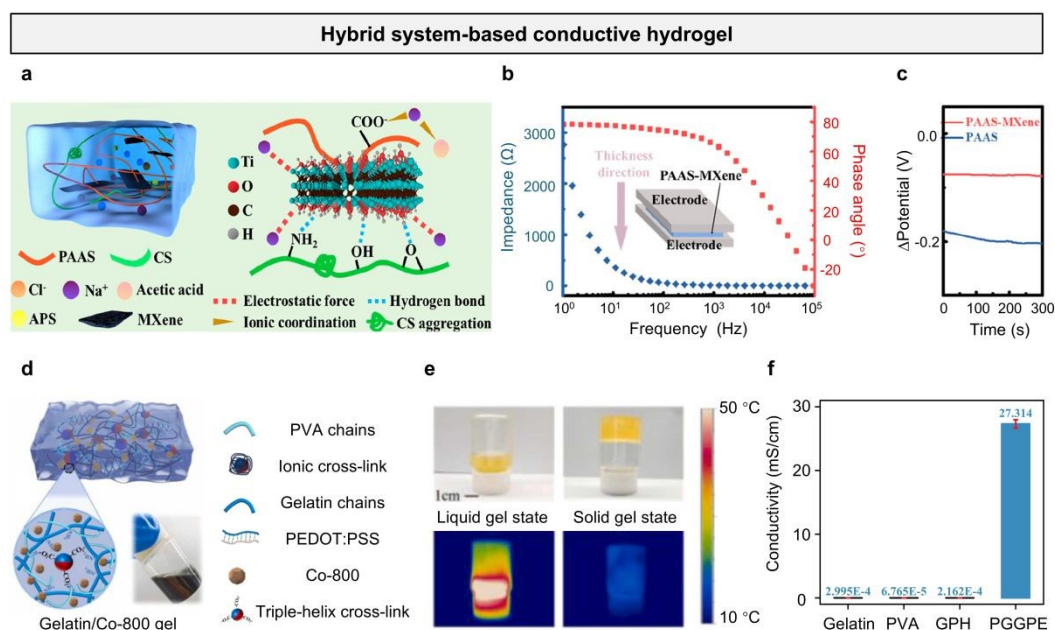


Fig. 4 Hybrid conductive-based conductive hydrogel. (a) Composition of PAAS-MXene cross-linked by single-layer MXene. (b) Electrical impedance of Bode plot in the thickness direction of PAAS-MXene hydrogel. (c) Comparison of polarization potential values and polarization potential change values of PAAS and PAAS-MXene. Reproduced with permission [73]. Copyright 2022, American Chemical Society. (d) Schematic illustration of the multifunctional bio-hydrogel. (e) Conductivity of gelatin, PVA, GPH, and PEDOT:PSS/graphene/gelatin/PVA hydrogel. (f) Comparison of single heartbeat waveform recorded by hydrogel electrode and commercial electrode. Reproduced with permission [74]. Copyright 2023, Wiley-VCH.

Wang et al.⁷⁵ developed a hybrid conductive hydrogel leveraging the synergistic effects of PEDOT:PSS/graphene and Na^+ ions (Fig. 4d). The hydrogel (GPH), composed of a dual-crosslinked network of gelatin and polyvinyl alcohol (PVA), exhibits a unique thermally responsive reversible phase transition between a flowable fluid state and a viscoelastic gel state (Fig. 4e). Compared to pristine hydrogels (6.76×10^{-5} mS/cm), the conjugated structure of PEDOT:PSS in the hybrid conductive hydrogel facilitates electron mobility, while graphene sheets form a conductive network that supports



efficient electron and ion transport. This results in significantly enhanced electrical conductivity, reaching 27.31 S/cm (Fig. 4f).

3. Properties of Conductive Hydrogel-based Epidermal Electrodes

To fulfill the essential requirements for electrophysiological signal monitoring, conductive hydrogel-based epidermal electrodes can be engineered with tailored properties, including conductivity, stretchability, and adhesion, using diverse synthesis and fabrication techniques (Table 1). This section outlines the essential properties required for conductive hydrogel epidermal electrodes, highlighting their critical role in ensuring the efficacy and reliability of electrophysiological monitoring.

Table 1 Summary of conductive hydrogel-based epidermal electrodes from different conductive mechanisms.

Conductive types	Hydrogel matrix	Conductivity materials	Conductivity (Test method)	Stretchability (%)	Adhesion (kPa)	Biocompatibility	Electrophysiological signals	Ref.
Ionic	AM/BIS/Water	NaCl	1.3 S/m (EIS)	1326	14	-	ECG/EEG	76
	AAM/PEGDA/Water	LiCl	0.01 S/m (EIS)	2500	-	-	EOG/EEG	77
	PVA/b-PEI/Water	CaCl ₂	3.09 S/m (EIS)	1291	10	-	ECG/EMG/EEG	78
	EGDMA/Water	VBIn-NTf ₂	0.0065 S/m (AC Resistance)	200	~400	-	ECG	79
	HEMA/SBMA/MBA/Water	LiTFSI	3 S/m (Four-point Probe)	287	7.5	High	ECG/EMG	80
	PAM/PDDA/Water	PMAANa	-	1000	19.2	-	ECG/EMG	57
	DMAEA/MBA/KPS/Water	ZM	-	1880	400	High	ECG/EMG	81
	AAM/LMA/KPS/Water	-	-	1410	-	High	ECG/EMG	82
	PVA/PAM/F-SiO ₂ /Water	CaCl ₂	10.58 S/m (EIS)	1450	26	-	ECG/EMG	83
	Gelatin glycerol/Borax/Water	Na ₂ SO ₄	9.3 S/m (EIS)	696	176	-	ECG/EMG/EEG	49
	Proanthocyanins/Guar gum/CNF/Water	FeCl ₃	0.023 S/m (Four-point Probe)	-	7.9	-	ECG/EMG	84
Electronic	EG/AAm/MBA/Water	DES	1.6 S/m (AC Resistance)	1660	0.01	High	ECG/EMG	85
	PVA/PDA/Water	PEDOT:PSS	2.18 S/m (Four-point Probe)	535	197	-	EMG	86
	PDA/Water	PEDOT:PSS	4 S/m (AC Resistance)	1300	22.4	High	ECG/EMG	87
	PVA/SA/APS/FeCl ₃ /Water	PEDOT:PSS	0.256 S/m (EIS)	334	-	-	ECG/EMG/EEG	88
	NIPAm/HEA/Water	poly(Cu-arylacetylide)	3.1 S/m (EIS)	108	43	High	ECG/EMG	89
	APS/SA/MBAA/KCl/CaSO ₄ /Water	PEDOT:PSS	-	50	64	High	EEG	90
	PAM/AM/Silk fibroin/Water	MXene	0.25 S/m (AC Resistance)	1560	29	-	EMG/EOG	91
	TA/ACC/Water	LM	0.02 S/m (EIS)	1000	28.9	High	ECG/EMG	92
	PVA/Borax/Water	PEDOT:PSS	0.002 S/m (Two-point Probe)	10000	15.7	-	ECG/EMG	93
	PAA/AlNO ₃ /Water	MXene	0.7 S/m	2400	494.2	-	ECG/EMG	94
	PAA/PVA/Water	RGO	0.11 S/m (Two-point Probe)	-	5.4	High	ECG/EMG/EOG	95
Hybrid	PAM/Alginate/Water	Ag	37400 S/m (Four-point Probe)	250	-	-	EMG	71
	PEGDA/Water	PEDOT:PSS/SBMA	0.03 S/m (EIS and DC Resistance)	390	6.5	High	ECG/EMG	69
	PAA/SA/AD/ADQ/Water	MXene/LiCl	1.8 S/m (EIS)	800	~27	High	ECG	96
	HA/Water/Glycerin	GNs/KCl/NaCl	0.33 S/m (EIS)	-	~5.5	High	EEG	97
	PEDOT:PSS/Fe/Water	PEDOT:PSS/Fe	1.25 S/m (EIS)	15	-	High	ECG	98
	PAA/TOCNFs/Water	PEDOT:PSS/Al(TFSI) ₃	7.1 S/m (EIS)	770	28	High	ECG/EMG	99
	PVA/Water	PPy/FeCl ₃	80 S/cm (Four-point Probe)	36	-	High	EMG	100

BIS: N,N'-Methylenebisacrylamide; PEGDA: poly(ethylene glycol) diacrylate; HEMA: 2-Hydroxyethyl methacrylate; SBMA: [2-(Methacryloxy) ethyl] dimethyl-(3-sulfo-propyl) ammonium



hydroxide; MBA: N,N'-Methylenebisacrylamide; SBMA: zwitterionic [2-(methacryloyloxy)ethyl]dimethyl-(3-sulfopropyl); LiTFSI: bistrifluoromethanesulfonimide lithium salt; PDA: polydopamine; NIPAm: N-isopropylacrylamide; HEA: 2-hydroxyethyl acrylate; GNs: graphite nanoparticles; HA: hyaluronic acid; DMAEA: 2-(Dimethylamino) ethyl acrylate; MBA: N,N'-methylenebis(acrylamide); KPS: potassium persulfate; LMA: lauryl methacrylate; ACC: calcium carbonate. EIS: electrochemical impedance spectroscopy.

3.1 Conductivity

The conductivity of hydrogel-based epidermal electrodes significantly influences the performance of bioelectronic interface electrodes, crucial for enabling efficient electrical signal transmission between biological tissues and electronic components while ensuring stable electrophysiological communication¹⁰¹. The polymer network serves as a structural scaffold, while the conductive fillers confer electrical conductivity to the hydrogel^{32, 102}. To date, a range of conductive materials, encompassing both electronic and ionic conductive fillers, have been employed in the fabrication of conductive hydrogels for epidermal electrodes¹⁰².

Ionic conductive fillers are incorporated into hydrogel systems by introducing acids (e.g., HCl, H₂O₄, H₃O₄, ionic compounds (e.g., LiCl, FeCl₃, AlCl₃, NaOH, KOH), or ionic liquids (e.g., 1-ethyl-3-methylimidazolium sulfate), which release free ions to significantly enhance electrical conductivity^{41, 103}. For instance, Zhang et al.¹⁰⁴ prepared highly conductive hydrogels by adding KOH and NaOH to a carboxymethyl chitosan (CECT)/PAM-based hydrogel (CTA). The ionic conductivity of the hydrogel samples was measured using electrochemical impedance spectroscopy, with conductivity ranging from 0.38 to 0.62 S/m.

Another way to achieve high conductive performance is typically to incorporate electronic conductive fillers (such as intrinsically conductive polymers, metal nanoparticles, or carbon-based nanomaterials) into hydrogels^{105, 106}. A typical example is that Wang et al.¹⁰⁷ employed a synergistic approach combining freeze-drying and



374 salting-out treatment to prepare a conductive hydrogel composite based on silver
375 nanowires (AgNWs) and PVA (Fig. 5a). This method successfully constructed a
376 layered hydrogel structure and significantly enhanced the local concentration of
377 AgNWs by inducing continuous phase separation. The resulting conductive hydrogel
378 composite exhibited remarkable properties, including ultra-high conductivity, excellent
379 stretchability (480% strain), and outstanding biocompatibility. The phase separation of
380 PVA in the hydrogel evolves with the extension of the salting-out time. By optimizing
381 the salting-out treatment time, the researchers successfully controlled the phase
382 separation process, resulting in a hydrogel with a conductivity exceeding 1739 S/cm
383 (Fig. 5b). Due to the high concentration of AgNWs, the prepared hydrogel still
384 maintains high conductivity under stretching, which is superior to other types of
385 hydrogels (Fig. 5c). Zhang et al.¹⁰⁸ developed a liquid metal (LM)-doped PVA-LM
386 hydrogel, incorporating LM microdroplets within a tannic acid (TA)-modified PVA
387 matrix (Fig. 5d). LM microdroplets were employed as crosslinkers to enhance
388 mechanical properties while providing exceptional conductivity, reaching a peak value
389 of 217895 S/m. The sedimentation time of LM profoundly influences the hydrogel's
390 conductivity, with the non-sedimented PVA-LM hydrogel exhibiting a significantly
391 lower conductivity of 0.004 S/m. After a sedimentation time of 30 minutes, the
392 conductivity of the PVA-LM hydrogel surged by five orders of magnitude to 455 S/m,
393 reflecting significant LM microdroplet precipitation (Fig. 5e). The PVA-LM hydrogel
394 was subjected to resistance measurements over 1200 stretching cycles (40% strain),
395 during which its resistance progressively decreased from 4.8 to 4.5 Ω (Fig. 5f). This
396 suggests mechanical sintering of LM microdroplets on the hydrogel surface under
397 external forces, concurrently enhancing its conductivity.

398 For epidermal electrodes, both ionic and electronic conductivity are essential yet
399 functionally distinct. Ionic conductivity plays a crucial role in interfacing with the skin,
400 which is a naturally ionic medium. Hydrogels with high ionic conductivity can form
401 low-impedance, conformal contacts with the stratum corneum, facilitating effective



coupling with bioelectric signals such as ECG, EMG, or EEG. This enables stable, high-fidelity acquisition of weak biopotentials with reduced signal loss or distortion.

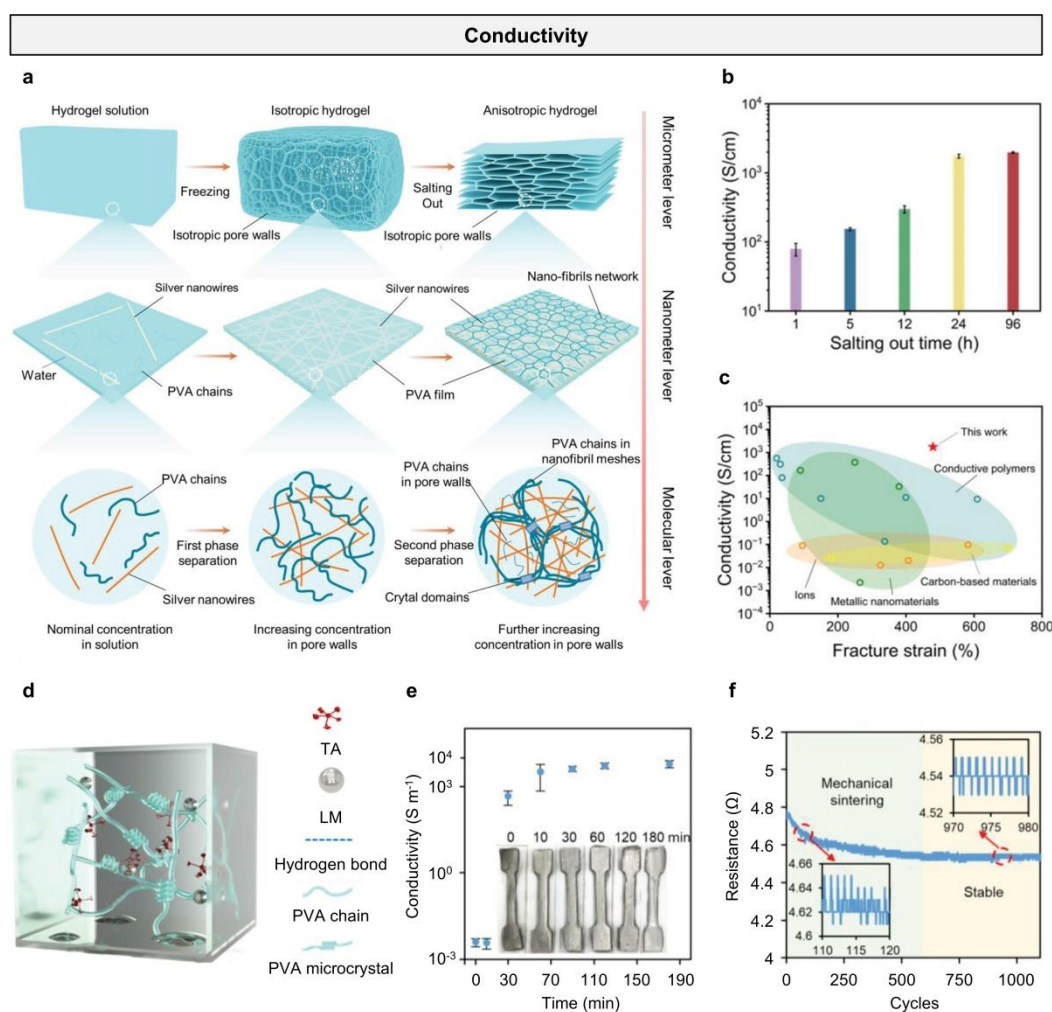


Fig. 5 Conductivity. (a) Schematic illustrating the fabrication procedure of AgNWs-PVA hydrogel composites by combining freezing and salting-out treatments. (b) Conductivity of the AgNWs-PVA hydrogel composites with varying durations of salting-out treatment. (c) Comparison of conductivity and fracture strain of the Ag-PVA hydrogel with other conductive hydrogels based on different conductive fillers. Reproduced with permission [107]. Copyright 2024, Wiley-VCH. (d) Schematic of PVA-LM hydrogel network. (e) Conductivity of PVA-LM hydrogels with different aging times. (f) The resistance response of PVA-LM hydrogel under cyclic stretching for 1000 cycles. Reproduced with permission [108]. Copyright 2024, Wiley-VCH.

Conversely, electronic conductivity is vital for rapid and efficient transmission of the collected signals to external readout devices. Materials such as PEDOT:PSS, CNTs, or MXene can form continuous electron pathways that minimize resistance across the electrode structure. In hybrid conductive hydrogels, the synergy between these two



conduction mechanisms enables high SNR, reduced motion artifacts, and stable performance under varying environmental and mechanical conditions. By combining the skin-compatible interface of ionic systems with the robust signal transfer capability of electronic systems, hybrid hydrogels offer a balanced and integrated solution for long-term, reliable epidermal bioelectronic applications.

3.2 Adhesion

Superior adhesive properties enable hydrogel-based epidermal electrodes to effectively adhere to the skin, minimizing skin-contact impedance and enhancing the quality and stability of monitored signals¹⁰⁹. To enhance the adhesive properties of conductive hydrogel-based epidermal electrodes, there are three typical mechanisms to enhance the adhesiveness of conductive hydrogel epidermal electrodes: physical adhesion, chemical adhesion, and biomimetic strategies¹¹⁰. In physical adhesion, external stimuli, including pH variations¹¹¹, temperature fluctuations¹¹², ultraviolet light¹¹³, magnetic fields¹¹⁴, and electric fields¹¹⁵, can be utilized to modulate the adhesive properties of hydrogels. A typical example is that Liu et al.¹¹⁶ proposed an electro-adhesion strategy with electrically programmable strength for universal and super-strong hydrogel bonding. The hydrogel is composed of PAA-Fe-Li. Owing to the robust hydration capacity of Li⁺ ions, they significantly modulate polymer chain interactions within the hydrogel, thereby enhancing its interfacial bonding through surface diffusion and accumulation (Fig. 6a). Driven solely by entropy related to the concentration gradient of the involved ions, PAA-Fe-Li exhibits effective adhesion to PVA hydrogels. After 5 seconds of contact, the adhesion strength and adhesion energy reach 0.24 MPa and 660 J/m², respectively. Subsequently, under a positive DC voltage, the adhesion efficiency of PAA-Fe-Li to PVA at ambient temperature significantly increased by ≈ 24 times (Fig. 6b). The peak adhesion strength and adhesion energy of PAA-Fe-Li with PVA substrates can reach 1.2 MPa and 3750 J/m², respectively. Adhered PAA-Fe-Li and PVA samples with a cross-sectional diameter of 6 mm can withstand at least 5 kg of



weight (Fig. 6c).

In chemical adhesion, the adhesive effect is mainly caused by chemical bonding and/or non-covalent interactions between reactive groups in the hydrogel and on the skin surface^{110, 117}. Covalent bonds play a predominant role in hydrogel adhesion due to their higher bond energy relative to other interactions¹¹⁸. Non-covalent interactions, including hydrogen and ionic bonds, are extensively employed in the fabrication of

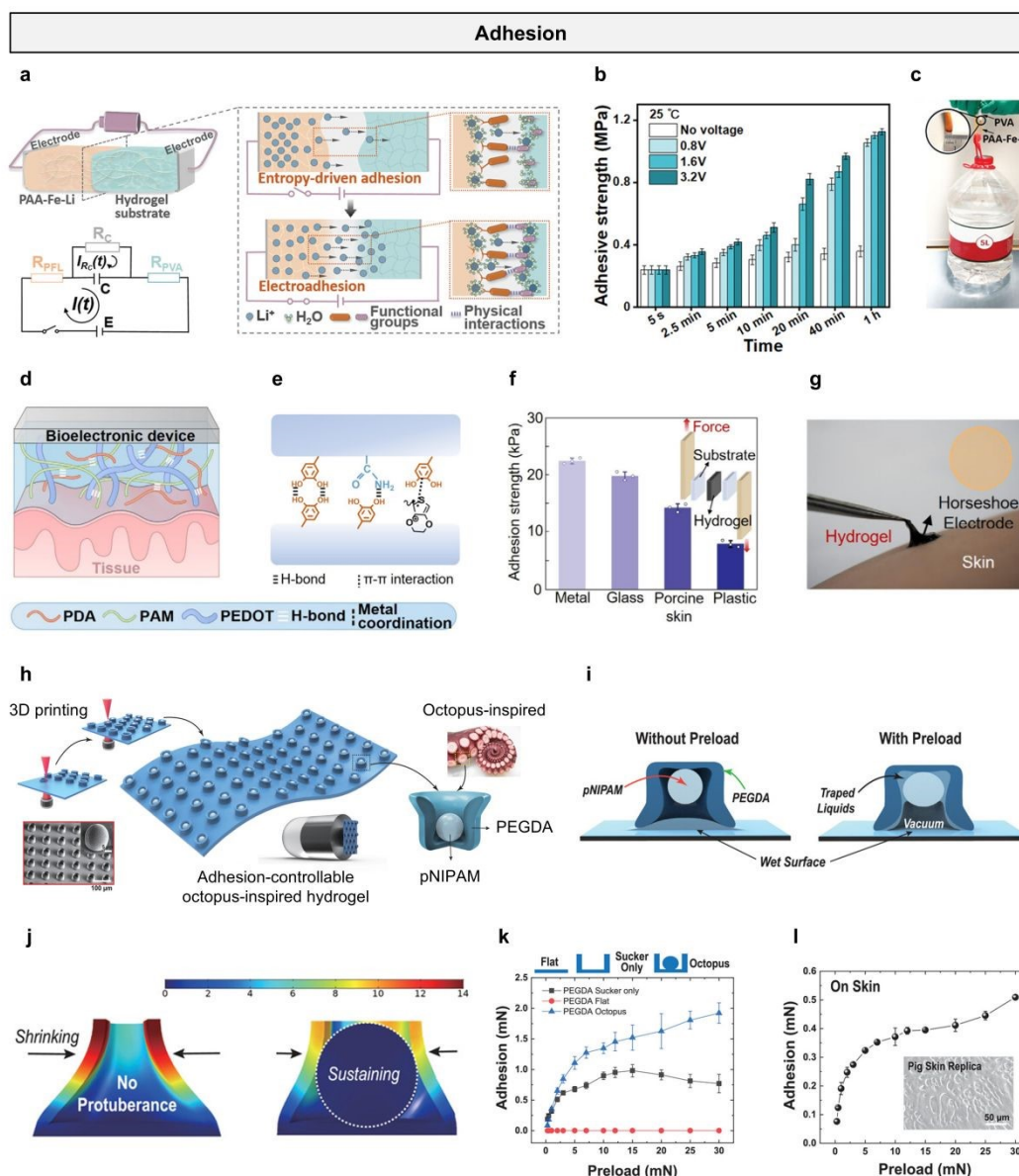


Fig. 6 Adhesion. (a) Mechanisms for strong interfacial bonding between the PAA-Fe-Li hydrogel and hydrogel substrate and schematic illustration of the proposed circuit model for electro-adhesion. (b) Adhesive strength of electro-adhesion between PAA-Fe-Li and PVA hydrogels at 25 °C. (c) Strong adhesion (> 5 kg) demonstration between PAA-Fe-Li and PVA. Reproduced with permission [116]. Copyright 2022, Wiley-VCH.



(d) Schematic illustration of a conventional bioelectronic device adhering directly to tissue. (e) Noncovalent interactions among dopamine methacrylate, PEDOT, PDA, and PAM chains. (f) Adhesion strength of hydrogel to different substrates by lap shear test. (g) Image of a hydrogel bioelectronic device for EMG and ECG monitoring. Reproduced with permission [87]. Copyright 2025, American Chemical Society. (h) Fabrication process of a polyethylene glycol diacrylate hydrogel. (i) Schematic illustration with finite element method simulation showing the adhesion mechanism of the sucker architecture with and without the inner protuberance structure. (j) Representative time-dependent profiles of adhesion results for the hydrogel patterns and flat glass for comparison. (k) Adhesion forces for different preloads (0.3–30 mN) in the samples of the inner pNIPAM and outer pNIPAM. (l) Adhesion results for different preloads (0.3 to 30 mN) in underwater conditions measured on the pig skin replica shown in inset. Reproduced with permission [119]. Copyright 2022, Wiley-VCH.

adhesive hydrogels to enhance interfacial adhesion¹²⁰. Hydrogen bonds, distinguished for their adjustable strength, biocompatibility, and reversible bonding capabilities, represent a key intermolecular force. Generally, individual hydrogen bonds in hydrogels are weak, necessitating their synergistic combination with other interactions or the formation of multiple hydrogen bonds to enhance adhesion¹²¹. For example, Lao et al.⁸⁷ developed a hydrogel with inherent adhesion and conductivity by integrating PAM-polydopamine (PDA) into conductive PEDOT, exhibiting a tissue-mimetic modulus (Fig. 6d). The adhesion is formed through non-covalent interactions of hydrogen bonds and π - π interactions with polydiacetylene and PAM chains (Fig. 6e). The shear strength of the hydrogel, adhered to various substrates including metal, glass, pig skin, and plastic, was measured at 22.4, 19.8, 14.2, and 7.9 kPa, respectively (Fig. 6f). Due to its ultra-soft and strong adhesive properties, the conductive hydrogel epidermal electrode can form a tight and robust interface with human tissue, thereby reducing artifacts caused by body movement (Fig. 6g). In biomimetic structures, the adhesion mechanisms of various organisms (including tree frogs, mussels, octopuses, and geckos) have attracted numerous researchers and inspired the development of biomimetic hydrogels^{122, 123}. For instance, the eight arms of an octopus are equipped with numerous suckers, each generating negative pressure via muscle control to produce robust adhesion¹²⁴. This mechanism, independent of chemical adhesives,



enables secure attachment to wet or irregular surfaces, such as marine rocks or prey. These attributes inspire the development of high-performance, reusable biomimetic adhesive materials tailored for complex environments. Inspired by the octopus's orifice, Lee et al.¹¹⁹ printed polyethylene glycol diacrylate (pNIPAM) hydrogel to form an outer wall, completing an internal dome-shaped structure mimicking octopus protrusions, which enhanced dry and wet adhesion (Fig. 6h). The pNIPAM achieves robust wet adhesion under external preload by inducing cohesive forces among liquid molecules at interacting wet surfaces (Fig. 6i and 6j). Due to the enhancement of suction, the sucker with an internal dome-like protrusion structure can enhance adhesion in wet environments (Fig. 6k). Adhesion was evaluated under preloads ranging from 0.5 to 30 mN on a skin-mimicking surface. Owing to the roughness of pig skin, adhesion on pig skin was approximately three times lower or more than that on a smooth glass surface (Fig. 6l).

3.3 Stretchability

Beyond essential conductivity and adhesion, superior tensile performance is a critical attribute that positions hydrogels as ideal materials for stretchable epidermal electrodes. This capability allows hydrogel-based electrodes to effectively accommodate body deformations while sustaining conformal contact, ensuring reliable signal transmission²⁷. Typical strategies for enhancing the mechanical properties of hydrogel epidermal electrodes include constructing multiple crosslinked network structures, adding nanocomposites, introducing supramolecular interactions, etc^{102, 125}. For example, Zhang et al.¹²⁶ developed an all-cellulose hydrogel with exceptional stretchability by introducing supramolecular structures through the ring-opening reaction of cellulose's anhydroglucose units via dehydration (Fig. 7a). The hydrogel's tensile properties were enhanced by modifying the cellulose structure and tuning interchain interactions. To increase chain flexibility, periodate oxidation was employed to selectively cleave the C2–C3 bond, converting secondary hydroxyl groups into



aldehyde groups and thereby opening the anhydroglucose ring structure. The resulting hydrogel exhibited a record-breaking tensile of 42200% strain. The mechanical properties of the hydrogel were significantly influenced by the content of diol cellulose nanorods (DCNRs). As the DCNR content increased from 23.3 to 28.8%, the tensile stress rose progressively from 7 to 25 kPa. When the DCNR content ranged from 23.3 to 28.8%, the strain of the hydrogels exceeded 10000% strain. (Fig. 7b). To further validate the hydrogel's stretchability, a 1 cm hydrogel was stretched to 4.42 m,

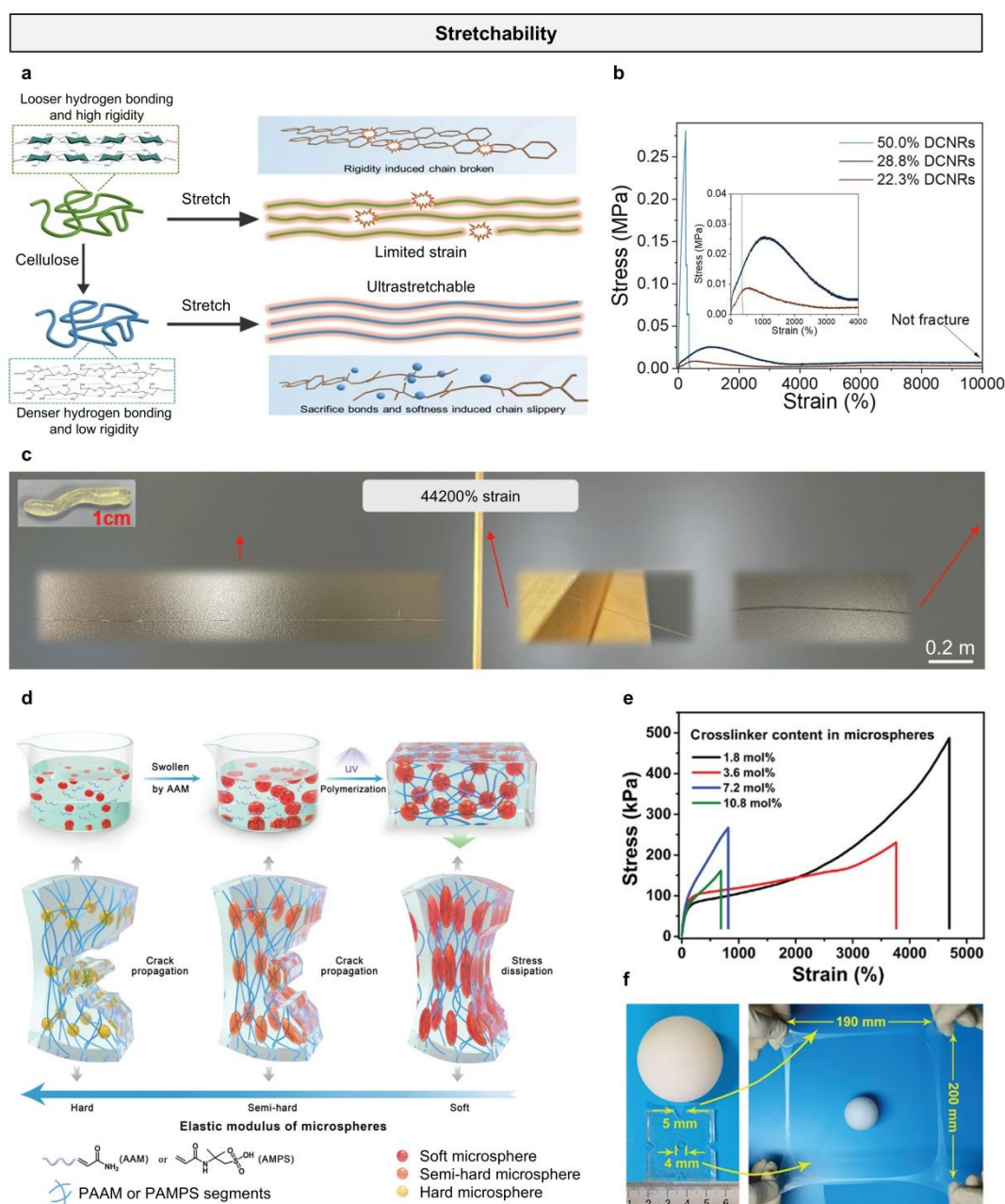


Fig. 7 Stretchability. (a) Schematic illustration of the cleavage of rigid anhydroglucose unit rings enhances hydrogel chain flexibility and facilitates the reformation of



hydrogen bonds during tensile deformation. (b) Stress-strain curves under different DCNRs contents. (c) Photos of DCNRs hydrogel before and after stretching. Reproduced with permission [126]. Copyright 2024, Wiley-VCH. (d) Schematic illustration of the preparation process and mechanism of super-stretchable hydrogel. (e) Tensile curves of hydrogels under different cross-linker concentrations. (f) Tear resistance of 5 mm long hydrogel under pre-cut equilateral triangle notch. Reproduced with permission [127]. Copyright 2022, Wiley-VCH.

corresponding to a strain of 42200% (Fig. 7c). Ji et al.¹²⁸ introduced an IL imidazolium salt with a urea backbone (UL) and incorporated sulfobetaine methacrylate (SBMA) and acrylamide (AM) into the hydrogel system (ULAS) through simple one-pot copolymerization. Supramolecular interactions within the IL strengthen the non-covalent bond network of hydrogel-based epidermal electrodes. As the IL concentration increases, the hydrogel exhibits markedly enhanced stress, achieving an elongation at break of 1075% strain and a fracture stress of 343 kPa. Constructing physically crosslinked, entangled, and micelle-crosslinked networks has been demonstrated as an effective way to enhance the mechanical properties of hydrogels. Li et al.¹²⁷ prepared a highly stretchable hydrogel with an interpenetrating entangled network by using PAM as the monomer and poly(1-acrylamido-2-methylpropanesulfonic acid) (PAMPS) as the physical crosslinking network, synthesized via UV-initiated free radical polymerization (Fig. 7d). The mechanical properties of hydrogels can be tuned by varying the crosslinker concentration. The fracture strain of hydrogels decreases rapidly with increasing crosslinking degree, reaching 4700% strain at a crosslinker content of 1.8 mol% (Fig. 7e). Furthermore, the hydrogel demonstrates outstanding tear resistance. Hydrogels with a 5 mm pre-cut notch extended to 190 mm and 200 mm under tensile stress without crack propagation. The area of a central circular pre-cut notch expanded approximately 2700-fold during cyclic biaxial stretching (Fig. 7f). Li et al.⁵⁴ developed a hydrogel with a multiply crosslinked network by incorporating gelatin and SA into PAM. With the addition of SA, a more complex network structure is formed between PAM/gelatin and SA through hydrogen bonds and electrostatic interactions between molecular chains. As the SA content rises from 0 to 0.8 wt%, the hydrogel's tensile stress increases from 61.3 to 229.3 kPa, with the elongation at break improving from



558 428.4 to 706.4% strain.

559 3.4 Gas-permeability

560 Water vapor and sweat accumulation at the skin-electrode interface can lead to skin
561 irritation and epidermal electrode failure during prolonged monitoring¹²⁹. Employing
562 gas-permeable conductive hydrogel-based epidermal electrodes has proven an effective
563 solution to this challenge¹³⁰. Common strategies for enhancing the gas-permeability of
564 conductive hydrogel-based epidermal electrodes include fabricating ultrathin and
565 porous structures^{129, 131}. A typical example is that Zhang et al.⁴⁹ introduced an ultrathin
566 polyurethane (PU) nanomesh-reinforced gas-permeable hydrogel. The hydrogel was
567 fabricated by immersing the PU nanomeshes in a temperature-sensitive gelatin-based
568 hydrogel solution (Fig. 8a). The resulting ultrathin hydrogel has a thickness of ~10.3
569 μm (Fig. 8b), with excellent mechanical strength (up to 696% strain) and high skin
570 adhesion (area adhesion energy of $176.8 \mu\text{J}/\text{cm}^2$). Owing to its ultrathin geometry and
571 porous structure, the hydrogel demonstrates a water vapor transmission rate (WVTR)
572 of $1669.3 \pm 23.5 \text{ g}/\text{m}^2/\text{day}$, closely comparable to that of an open bottle (1742.8 ± 18.3
573 $\text{g}/\text{m}^2/\text{day}$) (Fig. 8c). The resultant ultrathin hydrogel-based epidermal electrode enables
574 long-term, continuous, high-precision electrophysiological monitoring for up to 8 days
575 under everyday conditions.

576 Cheng et al.¹³² developed a cold lamination-based approach to fabricate breathable
577 hydrogel films with precisely controlled thickness and scalability. A mixed solution of
578 PAM and SA is cast between two polyethylene terephthalate (PET) support films and
579 then rapidly passed through the gap between two rollers. The prepared PET-wrapped
580 hydrogel precursor film is cured under ultraviolet light to complete in-situ gelation (Fig.
581 8d). The prepared hydrogel film thickness can be controlled to a minimum of $7 \mu\text{m}$.
582 The ultrathin hydrogel film has good skin conformability, and cross-sectional SEM
583 images show close contact between a fingerprint replica and a $10 \mu\text{m}$ thick hydrogel
584 film (Fig. 8e). Due to its ultrathin characteristics, the hydrogel film has good



breathability, measured by transepidermal water loss (TEWL). A 50 μm thick hydrogel film and a 3 μm thick impermeable parylene film were attached to the skin, respectively. After applying the ultrathin acrylic film for 2 hours, the initial skin hydration level increased from approximately 25 to 45%. Accompanying this, the TEWL significantly increased from ~ 7 to 12 $\text{g}/\text{m}^2/\text{day}$. After removing the acrylic film, the skin moisture level dropped to $\sim 28\%$ within 30 minutes, and the TEWL also decreased (Fig. 8f).

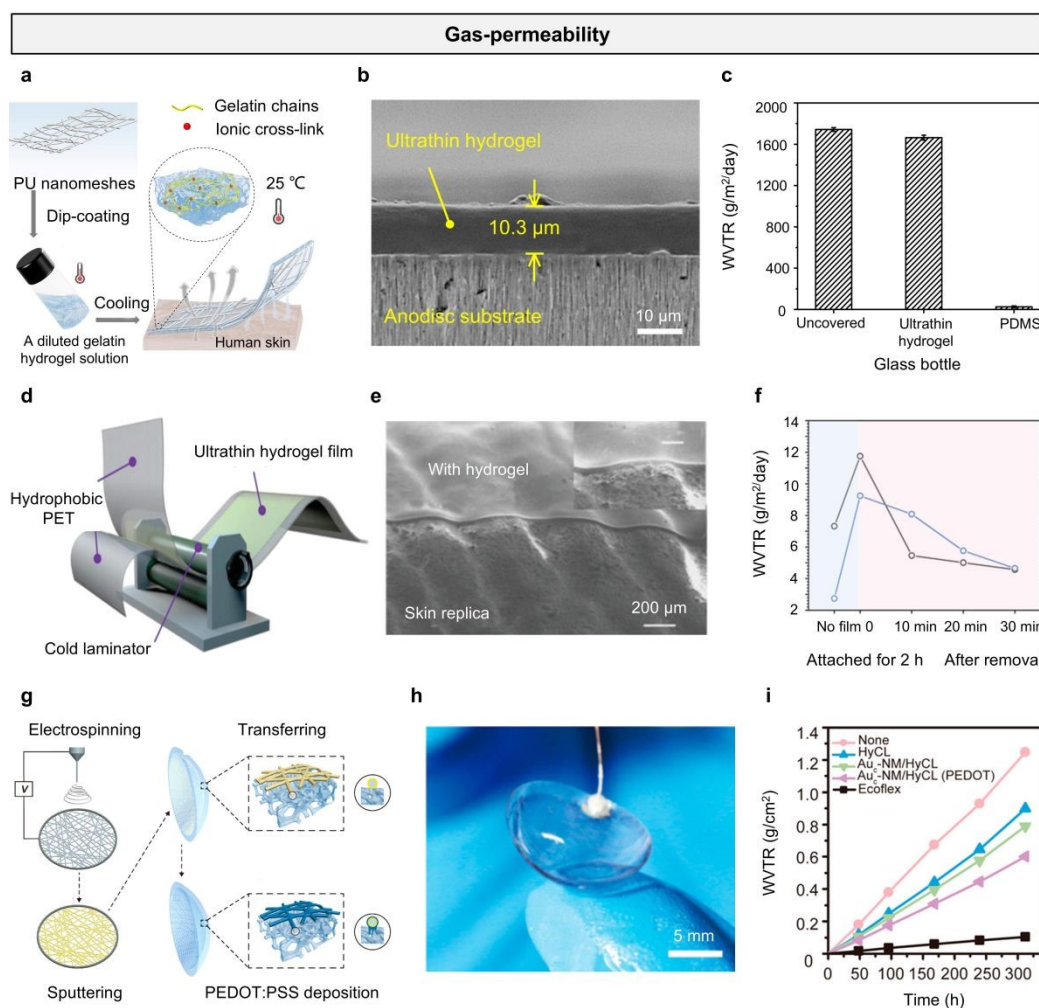


Fig. 8 Gas-permeability. (a) Schematic illustration of the design concept of PU nanomesh-reinforced hydrogels. (b) Cross-sectional SEM image of the ultrathin hydrogel attached on an anodisc substrate. (c) Comparison of WVTR for an uncovered bottle, a bottle covered with 1000- μm -thick PDMS film, and a bottle covered with ~ 10 - μm -thick ultrathin hydrogel, respectively. Reproduced with permission [49]. Copyright 2024, American Association for the Advancement of Science. (d) Schematic of the cold-lamination method to produce large-area ultrathin hydrogel films. (e) SEM images of a 10 μm thick hydrogel film attached to the fingerprint replica. (f) TEWL and the skin hydration level test by attaching a 3 μm thick parylene film on the forearm of the



601 volunteer. (g) Schematic illustration of the gas-permeable, irritation-free, transparent
 602 hydrogel film. Reproduced with permission [132]. Copyright 2022, Wiley-VCH. (h)
 603 Picture of a contact lens-based eye interfacing device based on the hydrogel film. (i)
 604 WVTR of open bottle (none), pure hydrogel ocular contact lens (HyCL), HyCL with
 605 gold-coated nanofiber mesh (Auc-NM/HyCL), Auc-NM/HyCL with deposition of
 606 PEDOT:PSS, and Ecoflex film as a function of elapsed time. Reproduced with
 607 permission [133]. Copyright 2019, American Chemical Society.

608 Wei et al.¹³³ reported a breathable, non-irritative, and transparent hydrogel film. The
 609 gas-permeable film was fabricated using a metal-coated nanofiber network (metal_c-NM)
 610 as the electronic conductor and a commercial hydrogel contact lens as the substrate,
 611 with in situ electrochemical deposition of PEDOT:PSS employing the metal_c-NM as
 612 the electrode (Fig. 8g). The resultant hydrogel film exhibits an optical transparency of
 613 90% (Fig. 8h). Owing to the highly porous structure of the metal_c-NM film, the
 614 underlying hydrogel substrate retains its breathability, enabling the hydrogel film to
 615 demonstrate excellent breathability with a WVTR of approximately 69.2 mg/cm²/day,
 616 significantly exceeding that of an impermeable Ecoflex film at 7.98 mg/cm²/day (Fig.
 617 8i).

618 4. Applications of Conductive Hydrogel-based Epidermal Electrodes in 619 Electrophysiological Monitoring

620 Conductive hydrogel-based epidermal electrodes, due to their good conductivity,
 621 outstanding skin adhesion and compliance, excellent stretchability, and superior
 622 breathability, have shown great potential in the field of electrophysiological signal
 623 monitoring. In this section, we will summarize the representative progress of
 624 conductive hydrogel-based epidermal electrodes in ECG, EMG, EEG, and EOG
 625 monitoring.

626 4.1 Electrocardiogram monitoring

627 ECG signals play a pivotal role in the medical field, being extensively utilized for



628 diagnosing cardiovascular diseases¹³⁴⁻¹³⁷, and assessing cardiac health^{138,140}.
629 Conductive hydrogel-based epidermal electrodes possess distinctive properties,
630 including high conductivity, excellent stretchability, and strong interfacial adhesion¹⁴¹,
631 ¹⁴². These attributes enable them to achieve superior SNR and sensitivity compared to
632 traditional rigid electrodes, thereby enhancing the accuracy and reliability of
633 monitoring and providing more precise data to support clinical diagnostics and
634 treatment.

635 A typical example is that Yang et al.¹⁴³ developed a wireless *Nepenthes*-inspired
636 hydrogel (NIH) hybrid system. The hybrid system consists of a skin electrode
637 assembled from a flexible circuit module, an electrode connector with a hollow
638 structure, a stretchable silicone joint, and three *Nepenthes*-inspired hydrogel interface
639 layers (Fig. 9a). The DN hydrogel based on PVA/PAA enhances its adhesion to the skin
640 (3.9 kPa). To evaluate the practicality of the NIH hydrogel system during motion, the
641 system was laminated on the skin above the subject's heart to collect ECG signals (Fig.
642 9b). To evaluate the stability of the NIH system, heart rate curves were recorded using
643 the system and a commercial device (i.e., Polar H10 heart rate strap) under motion
644 conditions, respectively. The results demonstrate that data from both systems reveal
645 nearly identical heart rate variation trends, with a relative deviation of less than 2.6%
646 over 5 minutes, validating the accuracy of the NIH system (Fig. 9c).

647 Inspired by the pentaradial symmetry of starfish, Chen et al.¹⁴⁴ introduced a starfish-
648 like wearable hydrogel-based bioelectronic system for high-fidelity ECG monitoring.
649 The skin interface layer consists of conductive hydrogels for five sensing pads and non-
650 conductive hydrogels for the central hub, while the serpentine arms remain independent.
651 The device is constructed on a 25 μm -thick polyimide (PI) substrate, utilizing copper
652 traces as conductive pathways. Its pentaradial design incorporates five serpentine arms,
653 each equipped with an independent sensing element at its tip, all linked to a central
654 electronic hub for data processing and wireless transmission. Signals are processed by
655 a 32-bit microcontroller and transmitted wirelessly, with analyzed data presented



Open Access Article. Published on 05 srpna 2025. Downloaded on 20.08.2025 13:06:50.
This article is licensed under a Creative Commons Attribution-NonCommercial 3.0 Unported Licence.



intuitively on a mobile device (Fig. 9d). By employing a conductive adhesive hydrogel
as the electrode-skin interface and a mechanically decoupled starfish-inspired device
design (Fig. 9e), this device enables high-fidelity ECG recordings across diverse
motion states, sustaining an SNR of approximately 35 dB even during running. The
system enables real-time, high-precision diagnosis of cardiac conditions by integrating
ECG, seismocardiogram, and gyrocardiogram signals with a deep learning model,
achieving classification accuracies of 91.31% for normal conditions, 94.03% for atrial

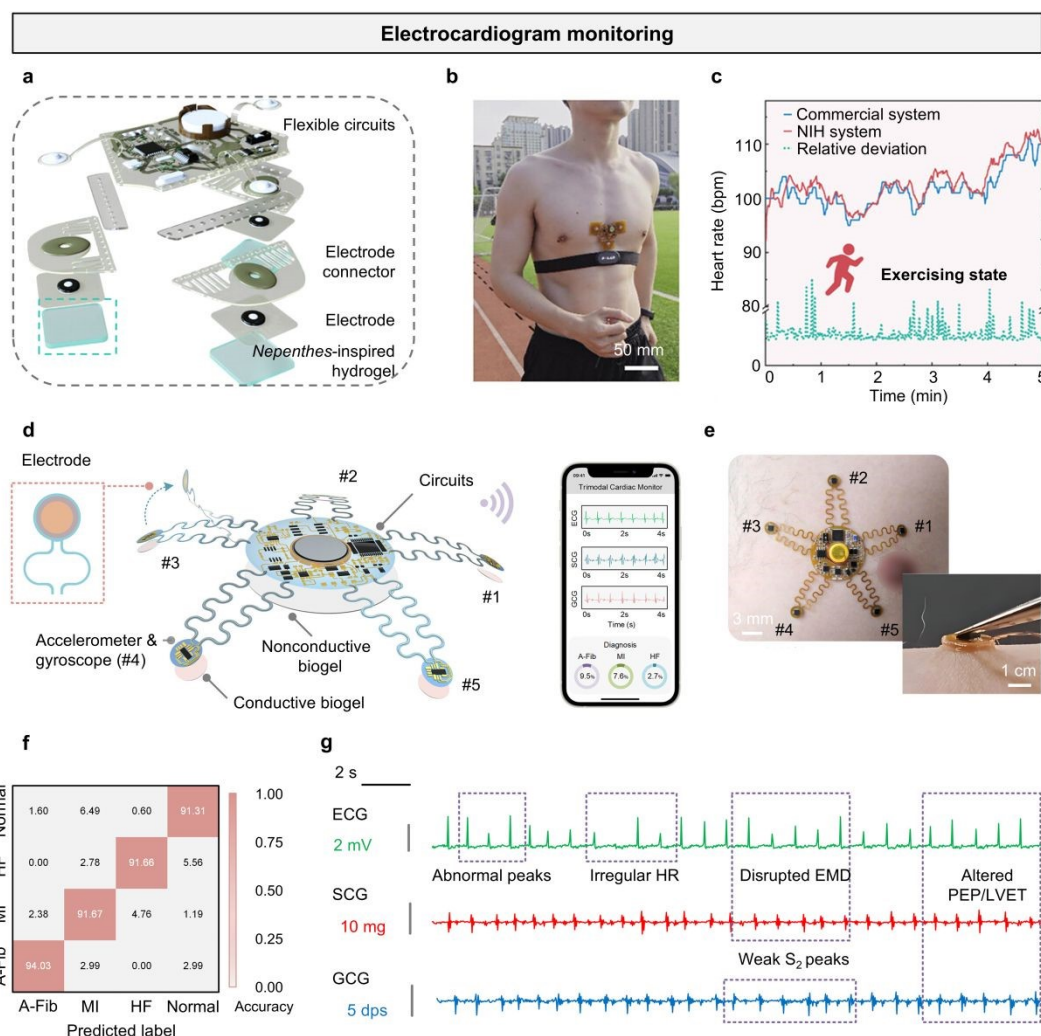


Fig. 9 Electrocardiogram monitoring. (a) Exploded 3D model of the NIH hybrid system. (b, c) Heart rate and relative deviation curves measured by the NIH system and commercial system under the subject's exercising states. Reproduced with permission [143]. Copyright 2024, Wiley-VCH. (d) Schematic illustration of the starfish-like device for trimodal cardiac monitoring during motion. (e) Optical image showing the device applied to the chest skin, with the five strategically positioned sensing pads, and optical image, showing robust adhesion of the sensing pad to human skin, facilitated by the conductive hydrogels. The image features a tweezer used to stretch the sensing pad

from the skin. (f) Confusion matrix, demonstrating the classification accuracy for predicting each type of heart disease and normal signals in the test set. During use, the starfish-like device can display the real-time classification probabilities on smart devices. (g) Cardiac electrical and mechanical signals collected by the starfish-like wearable device from a HF patient during walking; dps, degrees per second. Reproduced with permission [144]. Copyright 2025, American Association for the Advancement of Science.

fibrillation, 91.67% for myocardial infarction, and 91.66% for heart failure. Fig. 9f shows the cardiac mechanical and electrical biosignals captured by a hydrogel-based device during walking in a patient clinically diagnosed with heart failure. The signals show reduced Q and T peaks, irregular heart rate, interrupted electromechanical delay, and altered pre-ejection period/left ventricular ejection time parameters, indicating electrophysiological disturbances. Additionally, the patient's cardiac mechanical activity is significantly impaired, with a contraction amplitude nearly 60% lower than that of healthy individuals (Fig. 9g). These results demonstrate the ability of hydrogel-based epidermal electrodes to achieve high-fidelity recording of cardiac signals.

4.2 Electromyography monitoring

EMG is a technique for recording electrophysiological activity associated with muscle contraction and relaxation¹⁴⁵. As EMG signals directly reflect neuromuscular activity, they are extensively utilized in human motion monitoring¹⁴⁶⁻¹⁴⁸, controlling human-machine interfaces¹⁴⁹⁻¹⁵¹, and diagnosing neuromuscular disorders^{45, 152, 153}. However, the impedance between the electrode and skin affects the quality of EMG signals in practical applications, so researchers have increasingly focused on enhancing the conductivity and skin adhesion of hydrogel-based epidermal electrodes to achieve low interface impedance^{142, 154-157}. For instance, Tian et al.¹⁵⁸ leveraged the liquid-to-solid transition concept to develop an in-situ hydrogel-based epidermal electrode for monitoring post-fatigue muscle recovery (Fig. 10a). To develop a hydrogel with rapid in situ gelation, a formulation of gelatin, PEDOT:PSS, and a deep eutectic solvent (DES) was employed. At temperatures above 60 °C, gelatin exists as individual molecular



701 chains. Upon cooling, the gelatin network solidifies via hydrogen bonding and physical
 702 crosslinking, with PEDOT:PSS forming a conductive network within the gelatin matrix
 703 (Fig. 10b). DES demonstrate superior thermal stability and ionic conductivity. The
 704 hydroxyl groups in DES engage with the polymer network via hydrogen bonding and
 705 ionic interactions, improving solubility, stability, and network formation. The in situ-
 706 formed hydrogel exhibits exceptional adhesion (591 kPa) and minimal skin contact
 707 impedance (10.2 k Ω). The prepared in-situ biogel epidermal electrode was used to

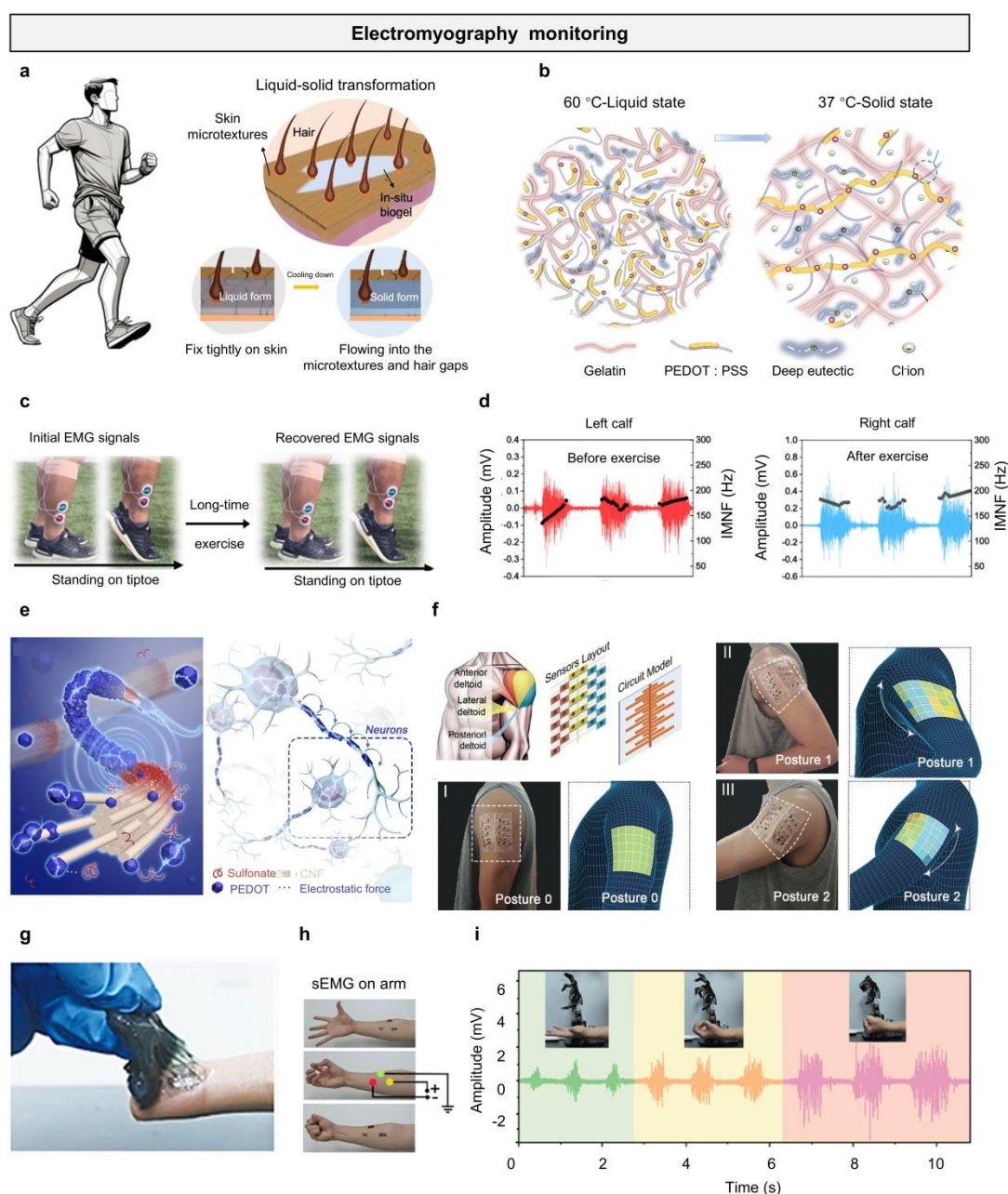


Fig. 10 Electromyography monitoring. (a) Liquid-to-solid transformation concept and the application of in situ biogel. (b) Schematic diagram and optical images of the



in situ rapid gelation process of the biogel. (c) Procedure for recovery monitoring using in situ biogel. Comparison of initial EMG signals with those after fatigue. (d) Initial EMG signals and post-exercise signals for left and right calves. Reproduced with permission [158]. Copyright 2025, Nature Publishing Group. (e) Schematic illustration of the biomimetic segmentally conductive fiber hydrogel. (f) Sensor array layout and circuit model designed for monitoring muscle movements. (j) Photograph of the self-adhesive hydrogel after peeling. (h, i) EMG signals on the forearm at different grip force levels. Reproduced with permission [99]. Copyright 2024, American Chemical Society.

monitor muscle recovery after exercise-induced fatigue. EMG signals from the left and right calves were recorded when volunteers performed toe-raising exercises (Fig. 10c). After prolonged exercise (running for 45 minutes), the hydrogel epidermal electrode recorded EMG signals at different stages, with an SNR of up to 30 dB (Fig. 10d). Hydrogel-based epidermal electrodes were employed to monitor muscle signals in volunteers during extended sedentary periods, revealing a decline in average muscle frequency over time. After 24 hours, the mean muscle frequency started to rise, approaching pre-exercise levels by 48 hours, signifying full recovery from exercise-induced fatigue. To quantitatively assess muscle fatigue recovery, the recovery percentage was defined as the ratio of mean EMG frequencies before and after exercise-induced fatigue. This recovery metric enables precise evaluation of muscle condition, supporting exercise and recovery planning, as well as monitoring recovery from muscle-related disorders. Liu et al.⁹⁹ designed high-performance hydrogel-based epidermal electrodes by incorporating numerous interpenetrating core-sheath conductive nanofibers into a physically crosslinked polyelectrolyte network. The hydrogel is composed of cellulose nanofibers, PAA, and PEDOT:PSS (Fig. 10e). The hydrogel-based epidermal electrode was fabricated as a $10 \times 10 \text{ cm}^2$ multi-pixel skin array, showcasing its capability to capture human motion across various postures (Fig. 10f). As an interface for human-machine interaction, the hydrogel epidermal electrode exhibits good interfacial adhesion (adhesion energy of 28 kPa on pig skin) and a low electrochemical impedance of 42 Ω . Fig. 10g shows that after peeling from the skin, a typical “fibrillation” phenomenon occurs, confirming effective adhesion between the



hydrogel epidermal electrode and the skin (Fig. 10h). To evaluate the human-machine interaction capability of the hydrogel epidermal electrode, the electrode was used to test EMG signals on the forearm under different grip strength levels, and the recorded arm EMG signals could be customized to precisely control a prosthetic limb, thereby achieving various robotic gestures with adjustable grasping angles and force levels (Fig. 10i).

4.3 Electroencephalogram monitoring

EEG is an electrophysiological monitoring method for recording brain electrical activity.¹⁵⁹ It mainly originates from postsynaptic potentials and has significant application potential in sleep monitoring¹⁶⁰⁻¹⁶², emotion recognition¹⁶³⁻¹⁶⁵, and brain-computer interfaces¹⁶⁶⁻¹⁶⁸. The presence of scalp hair and the head's intricate, curved contours pose significant challenges in achieving stable and effective contact between epidermal electrodes and the scalp for prolonged EEG recordings¹⁶⁹. To overcome this challenge, Wang et al.¹⁷⁰ developed a conductive gel-based epidermal electrode for skin application, featuring a temperature-responsive reversible liquid-to-gel transition. This phase transition endows the hydrogel with unique skin coating and in-situ gelation properties (Fig. 11a). The fluidity of the conductive hydrogel enables good compliance and conformal contact with hairy scalps without hair interference, surpassing prefabricated gels, which facilitates high-quality EEG recording through hairy scalps (Fig. 11b). The conductive hydrogel-based epidermal electrode was utilized to capture EEG signals during open-eye and closed-eye conditions, revealing distinct differences between the signals in these paradigms. Due to its relatively long-term electrical stability, excellent mechanical interaction (73.4 ± 2.2 kPa), and stable contact with the scalp (6.95 ± 0.97 k Ω), the conductive hydrogel epidermal electrode recorded α signals with no significant differences across different wearing durations (0, 24, 48, and 72 hours), with high quality and a peak frequency of 10 Hz (Fig. 11c). This indicates that the applicable conductive hydrogel epidermal electrode has promising capabilities for



View Article Online
DOI: 10.1039/D5TC01896J

long-term high-fidelity EEG recording. To enable continuous high-fidelity EEG signal
detection, paintable hydrogel-based epidermal electrodes require a streamlined and
rapid gelation process to minimize adhesion-related damage from slow gelation and
reduce subject discomfort. Li et al.¹⁷¹ developed a paintable, fast-gelling, and highly
adhesive hydrogel-based epidermal electrode via a one-pot synthesis. Comprising
gelatin, gallic acid, sodium citrate, LiCl, glycerol, and Tris-HCl buffer (Gel-GGLiCit),

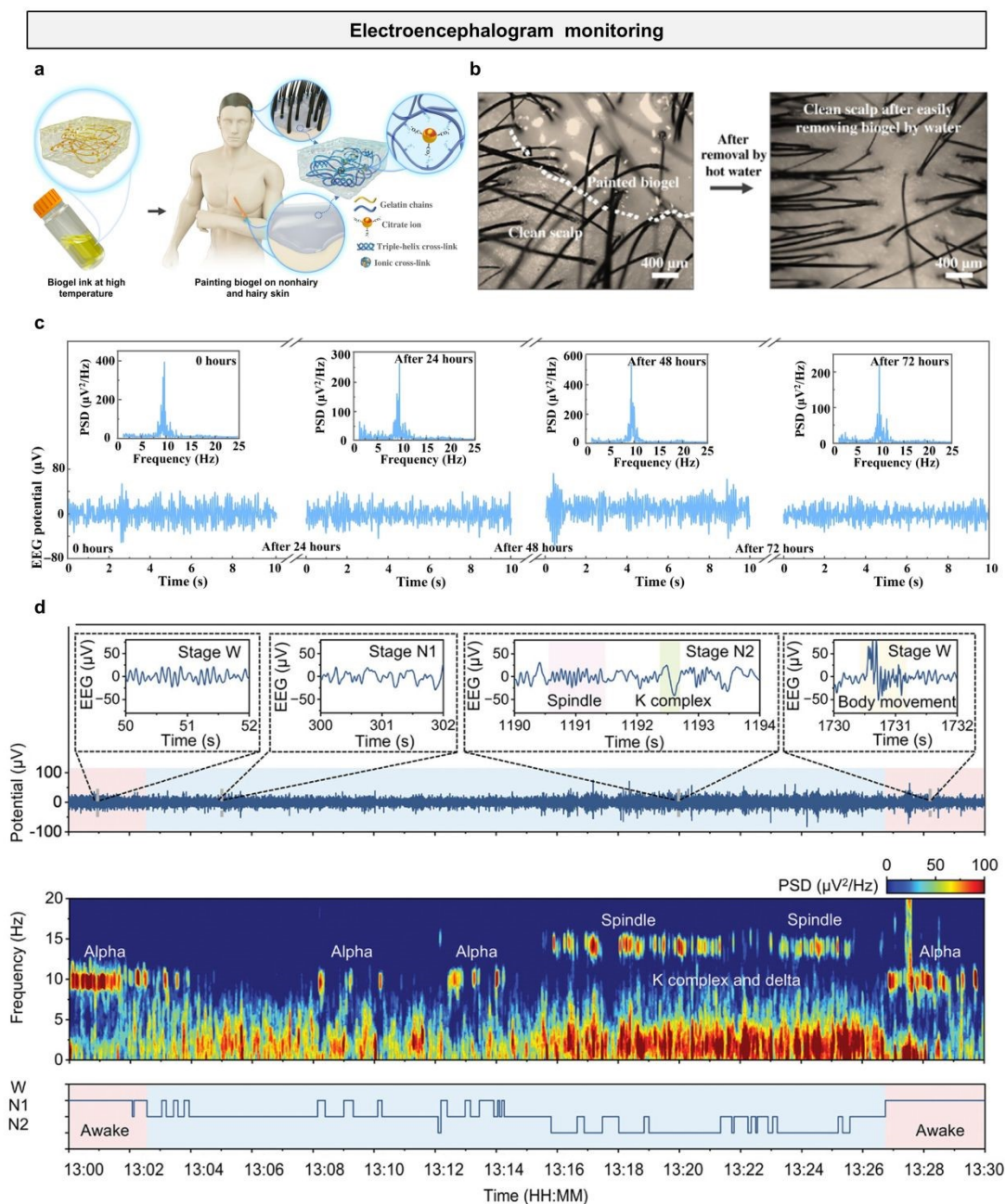


Fig. 11 Electroencephalogram monitoring. (a) Schematic illustration showing the concept of on-skin paintable biogel for hairy scalp for EEG recording. (b) Optical images of biogel painted on the hairy scalp and clean scalp after removing biogel by

water. (c) EEG alpha rhythms recorded by the painted biogel electrode after continuous wearing for 0, 24, 48, and 72 hours. Reproduced with permission [170]. Copyright 2022, American Association for the Advancement of Science. (d) Continuous wireless monitoring of EEG signals using paintable Gel-GGLiCit hydrogels and the multitaper spectrogram of the EEG signals (top) and visually scored hypnogram (bottom). Reproduced with permission [171]. Copyright 2024, Wiley-VCH.

the hydrogel possesses reversible thermal phase transition properties, facilitating skin compatibility and rapid in situ gelation within 15 seconds. Furthermore, the paintable hydrogel-based epidermal electrode can form a conformal interface with hairy scalps (3.36 mJ/cm^2) in its fluid state prior to gelation, allowing it to penetrate dense hair effectively. These properties substantially lower scalp contact impedance, with the electrode achieving a reduced skin contact impedance of $45.64 \text{ k}\Omega$ compared to $62.70 \text{ k}\Omega$ for commercial pastes. To assess the potential of the paintable hydrogel-based epidermal electrode for sleep stage monitoring and sleep disorder analysis, it was employed to capture EEG signals from subjects during brief daytime naps. In addition to the awake state, the subject's 30-minute sleep primarily involved non-rapid eye movement (NREM) sleep, stages N1 and N2. Stage N1 marks the initial phase of sleep, defined by the transition from wakefulness to sleep, where individuals experience light sleep and are easily roused. Following N1, stage N2 emerges as a deeper sleep phase, characterized by a reduced heart rate and the occurrence of sleep spindles (Fig. 11d). During the awake stage (W), elevated power in the alpha band (8–12 Hz) is evident in EEG signals, most pronounced during eye closure. As wakefulness transitions to stage N1, alpha band power progressively diminishes and eventually disappears. These findings demonstrate that high-fidelity raw EEG data, acquired with paintable hydrogel-based epidermal electrodes, enable clear visualization of critical EEG features throughout sleep.

4.4 Electrooculography monitoring

EOG is a technique that measures eye movement and position by recording electrical potentials around the eyes, widely used for diagnosing ophthalmic and neurological



disorders^{172, 173}, supporting human-computer interaction^{174, 175}, studying cognitive processes^{176, 177}, and assessing fatigue and alertness^{178, 179}. Zheng et al.¹⁸⁰ developed a thermoresponsive gelatin-based hydrogel (GGW) via a one-pot synthesis, incorporating glycerol, ammonium chloride (NH_4Cl), and water (Fig. 12a). The in situ-formed hydrogel electrode demonstrates robust adhesion at the hydrogel-skin interface (0.9 N/cm), enabling conformal skin contact and high-fidelity signal acquisition (Fig. 12b).

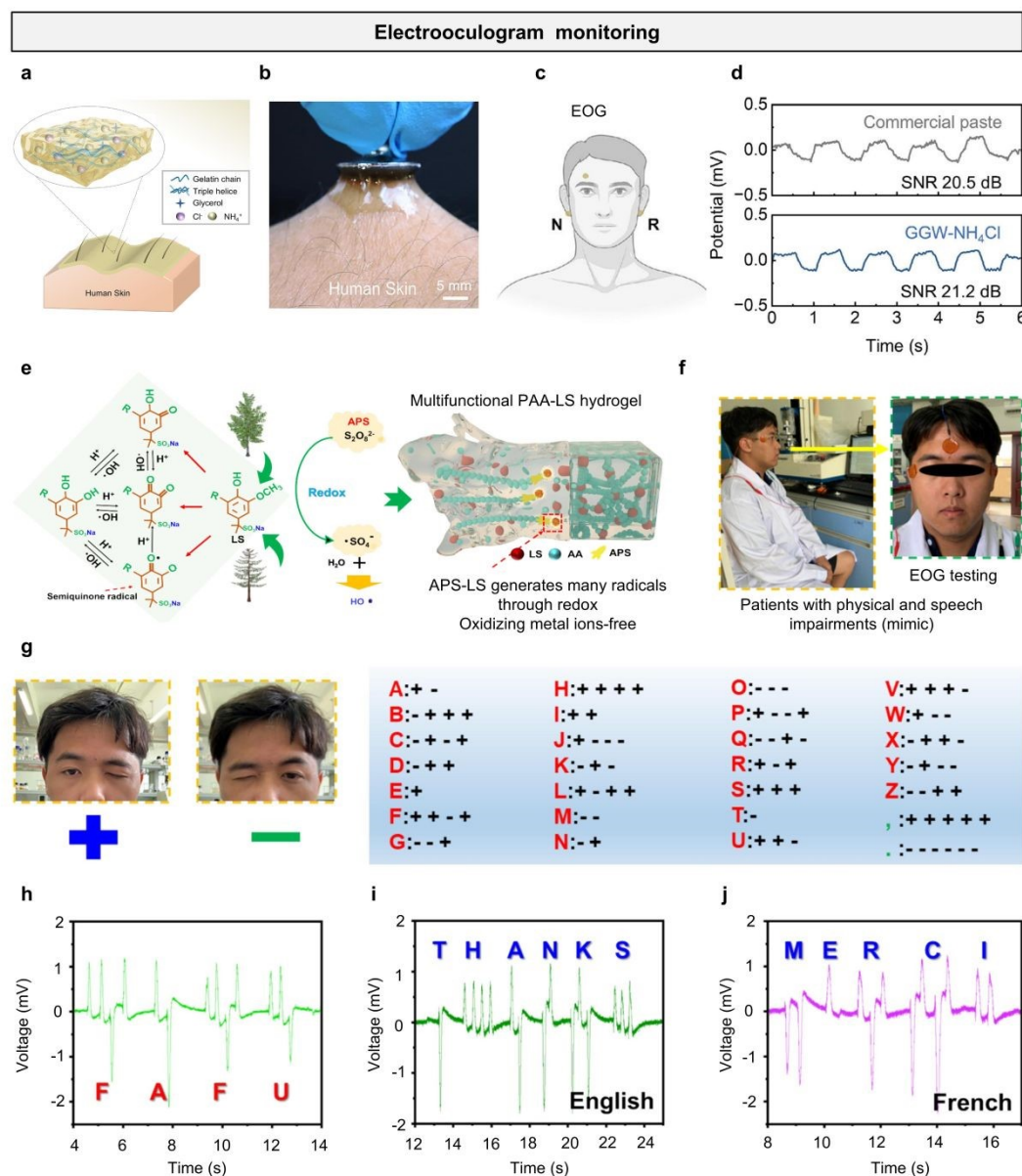


Fig. 12 Electrooculography monitoring. (a) Schematic view depicting the concept of a skin-printable hydrogel. (b) Photograph showing the attachment of Ag/AgCl electrode to the GGW- NH_4Cl hydrogel, highlighting the superior adhesion. (c) Schematic of electrode positions for EOG signal measurements. (d) EOG signals recorded using commercial paste (top) and the GGW- NH_4Cl hydrogel (bottom), along



820 with the corresponding SNR. Reproduced with permission [180]. Copyright 2025,
821 Elsevier. (e) Schematic illustration of the preparation, function, and application of
822 oxidative metal ions-free lignin-catalyzed hydrogels. (f) Schematic diagram of PAA-
823 LS-0.05 hydrogel-based bioelectrodes adhered to the skin of a volunteer's head for EOG
824 monitoring. (g) Schematic diagram of the codable eye communication mechanism. (h)
825 The gel electrodes detected the volunteers' eye movements, which the device
826 interpreted as the word "FAFU". This volunteer effectively produced the outputs i)
827 "thanks" and j) "merci" (French). Reproduced with permission [181]. Copyright 2025,
828 Elsevier.

830 The hydrogel was placed around the eyes for EOG signal monitoring, and then the
831 signals were transmitted through a Bluetooth-enabled portable wireless module for real-
832 time data collection. Fig. 12c illustrates representative EOG signals acquired with
833 hydrogel-based epidermal electrodes, exhibiting pronounced periodic waveforms as the
834 subject repeatedly shifts their gaze from side to side. Notably, the EOG signals obtained
835 using the hydrogel epidermal electrode exhibit higher amplitude than those recorded
836 using commercial paste. Meanwhile, the SNR (21.2 dB) of the hydrogel epidermal
837 electrode surpasses that of the commercial paste (20.5 dB) (Fig. 12d).

838 To validate the capability of the hydrogel epidermal electrode in acquiring EOG signals
839 from patients with speech impairments, Pan et al. reported a multifunctional PAA
840 hydrogel catalyzed by oxidative metal-ion-free lignin¹⁸¹. By incorporating transition
841 metal ions and sodium lignosulfonate (LS), LS rapidly reduces Fe^{3+} to Fe^{2+} , thereby
842 promoting the rapid generation of free radicals by APS (initiator) at room temperature.

843 This mechanism accelerates the polymerization of vinyl monomers, enabling the rapid
844 assembly of the hydrogel (Fig. 12e). The hydrogel exhibits excellent flexibility (~ 7 kPa),
845 remarkable stretchability ($\sim 2700\%$ strain), and strong skin adhesion (~ 9 kPa).

846 Notably, the hydrogel, integrating these superior properties, can serve as an epidermal
847 electrode for the human body, offering a viable alternative to conventional commercial
848 electrodes. Fig. 12f illustrates a volunteer wearing the PAA-LS-0.05 hydrogel
849 epidermal electrode undergoing an EOG test. The volunteer simulated a patient with
850 severe physical and verbal impairments, retaining only limited facial skin mobility and
851 lacking the ability to speak or type. To address this, the actions of closing the left and



852 right eyes were defined as “+” and “−”, respectively (Fig. 12g), and a reference table
853 comprising 26 English letters and punctuation marks was developed. Through regular
854 eye movements, the patient could achieve linguistic output and communication. As
855 shown in Fig. 12h, the patient successfully produced the unordered sequence “F A F
856 U” via eye movements, with the signal being clearly readable. Subsequently, the patient
857 further expressed the English word “THANKS” (Fig. 12i) and the French word
858 “MERCI” (meaning “thank you”, Fig. 12j) through eye movements. This wearable
859 hydrogel electrode seamlessly integrates with the eye-movement-based communication
860 system, offering a significant and urgent solution to address communication challenges
861 for such patients.

862 While conductive hydrogel-based epidermal electrodes have demonstrated excellent
863 performance across various electrophysiological modalities—including ECG, EMG,
864 EEG, and EOG—their practical deployment in dynamic, real-world environments
865 poses additional challenges related to signal stability and quality. Motion artifacts
866 remain a major concern in wearable and long-term bioelectronic monitoring, often
867 arising from skin deformation, electrode displacement, or body movement. These
868 artifacts can significantly distort low-amplitude biopotentials—particularly in EEG and
869 ECG recordings—thereby compromising signal fidelity and diagnostic accuracy. The
870 intrinsic softness, stretchability, and conformability of hydrogel-based electrodes help
871 maintain stable skin–electrode contact, effectively minimizing impedance fluctuations
872 and suppressing artifact generation at the source. Additionally, signal processing
873 techniques such as adaptive filtering, baseline drift correction, and motion-sensor-
874 assisted denoising are widely employed to further improve signal quality. Therefore,
875 the integration of material-level optimization and algorithmic post-processing is
876 essential for achieving reliable, high-fidelity electrophysiological recordings under
877 real-life conditions.



5. Summary and Perspectives

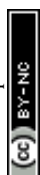
Conductive hydrogels, characterized by their intrinsic flexibility, tunable properties on adhesion and electrical conductivity, hold significant promise for the development of high-performance epidermal electrodes. This review offers a comprehensive overview of recent advances in conductive hydrogel-based electrodes for electrophysiological monitoring. We first examined the underlying conductive mechanisms—ionic, electronic, and hybrid pathways—followed by a discussion of the essential properties required for effective signal acquisition, such as high conductivity, strong adhesion, stretchability, and breathability. Finally, we highlighted recent progress in their application across various electrophysiological monitoring scenarios. Despite notable achievements, several challenges persist that must be addressed to fully realize their potential.

Advancements in materials and conductivity mechanisms

The future development of conductive hydrogel-based epidermal electrodes will be driven by innovations in materials science and the continued refinement of conductivity mechanisms. While current strategies largely focus on ionic, electronic, and hybrid conduction, future research will likely prioritize optimizing these mechanisms for enhanced signal fidelity and long-term stability. Incorporating advanced conductive polymers and nanomaterials could significantly improve electronic conductivity, overcoming the environmental sensitivity associated with ionic pathways. Additionally, bioinspired designs—such as the integration of conductive peptides or materials that mimic the skin's natural electrical properties—offer the potential for improved biocompatibility and seamless integration with biological systems. These innovations aim to produce electrodes capable of reliable, high-quality electrophysiological monitoring in dynamic and diverse conditions.

Strategies for long-term reliability

Long-term performance and durability of conductive hydrogel-based epidermal



electrodes can be greatly enhanced through advanced materials design and interfacial engineering. One promising direction is the development of fatigue-resistant architectures, such as self-healing polymer networks and dynamic crosslinking systems, which can maintain mechanical integrity under repeated deformation. Hybrid structures that combine elastomers with hydrogels may further improve stretchability and resistance to cracking. To address adhesion challenges under real-world conditions—such as perspiration, oily skin, or continuous body motion—bioinspired adhesive strategies present an exciting pathway. These may include catechol-functionalized chemistries, microstructured surface designs, or reversible covalent bonding, enabling robust and repeatable skin contact. Advances in hydration management are also expected to play a crucial role in maintaining performance over extended use. Future studies may explore the integration of moisture-retentive additives, breathable yet protective encapsulation materials, or systems capable of autonomous hydration regulation to prevent dehydration and ion leaching.

Multifunctionality and smart features

Beyond signal monitoring, the next generation of conductive hydrogel electrodes is expected to embrace multifunctionality and smart responsiveness. One promising direction is the development of closed-loop systems, where electrodes not only detect physiological signals but also trigger therapeutic interventions, such as on-demand drug delivery. Incorporating self-healing capabilities through dynamic covalent bonds or supramolecular interactions could greatly enhance durability, especially under mechanical strain during long-term use. Additional smart features—such as energy harvesting from body movement or adaptive behavior in response to skin conditions—could further extend the functionality and lifespan of these devices. These advancements will transform conductive hydrogels into versatile, intelligent platforms that bridge sensing, therapy, and human-machine interfaces.

Wearability, data integration, and personalized medicine

The long-term vision for conductive hydrogel-based epidermal electrodes lies in their



933 seamless integration into wearable systems that support comfort, continuous data
934 acquisition, and personalized healthcare. Innovations in material design—particularly
935 ultrathin, breathable, and skin-conformal hydrogels—will be crucial to improving
936 wearability and minimizing skin irritation during extended use. Simultaneously,
937 integrating these devices with advanced data analytics and machine learning algorithms
938 will unlock their potential for real-time monitoring, predictive diagnostics, and
939 personalized treatment strategies. This convergence of soft materials, digital health, and
940 precision medicine heralds a shift toward proactive, patient-centered care, where
941 electrophysiological monitoring becomes not just reactive but a key driver in managing
942 health and disease.

943 **CRedit Authorship Contribution Statement**

944 **Jiawei Yang:** Writing – origin draft, Writing – review&editing, Investigation, Data
945 curation. **Yi Liu:** Writing – origin draft, Writing – review&editing, Resources,
946 Methodology, Data curation. **Wenqing Yan:** Writing – review&editing, Formal
947 analysis. **Pengcheng Zhou:** Writing – review&editing, Formal analysis. **Zonglei**
948 **Wang:** Writing – review&editing, Formal analysis. **Yuli Wang:** Writing –
949 review&editing. **Yujie Zhang:** Writing – review&editing, Formal analysis. **Zongman**
950 **Zhang:** Writing – review&editing, Software. **Fan Mo:** Writing – review&editing.
951 **Zichong Ji:** Writing – review&editing. **Hossam Haick:** Writing – review&editing.
952 **Yan Wang:** Writing – review&editing, Project administration, Funding acquisition,
953 Conceptualization.

954 **Declaration of Competing Interest**

955 The authors declare that they have no known competing financial interests or personal
956 relationships that could have appeared to influence the work reported in this paper.



957 **Acknowledgments**

958 The authors sincerely acknowledge the support from the Natural Science Foundation
 959 of China (grant No.: 52303371, W2521021), Guangdong Science and Technology
 960 Department (grant Nos.: STKJ2023075, 2022A1515110209, 2021B0301030005), seed
 961 fund from GTIIT Changzhou Innovation Institute (grant No.: GCII-Seed-202406), and
 962 the Key Discipline (KD) Fund, the Technion, and the Start-Up Fund from Guangdong
 963 Technion.

964 **Notes and Reference**

- 965 1. Y. Xiang, K. Shi, Y. Li, J. Xue, Z. Tong, H. Li, Z. Li, C. Teng, J. Fang and N.
 966 Hu, *Nano-Micro Lett.*, 2024, **16**, 132.
- 967 2. J. P. Piccini, A. M. Russo, P. S. Sharma, J. Kron, W. Tzou, W. Sauer, D. S.
 968 Park, U. Birgersdotter-Green, D. S. Frankel and J. S. Healey, *Circulation:
 969 Arrhythmia and Electrophysiology*, 2022, **15**, e009911.
- 970 3. K. E. Odening, A.-M. Gomez, D. Dobrev, L. Fabritz, F. R. Heinzel, M. E.
 971 Mangoni, C. E. Molina, L. Sacconi, G. Smith and M. Stengl, *EP Europace*,
 972 2021, **23**, 1795-1814.
- 973 4. A. H. Caillet, A. T. Phillips, L. Modenese and D. Farina, *J. Electromyogr.
 974 Kinesiol.*, 2024, **76**, 102873.
- 975 5. R. Sun, A. Sohrabpour, G. A. Worrell and B. He, *PNAS*, 2022, **119**,
 976 e2201128119.
- 977 6. F. Arcuri, C. Porcaro, I. Ciancarelli, P. Tonin and A. Cerasa, *Electronics*, 2021,
 978 **10**, 836.
- 979 7. M. Pyasik, M. Scandola and V. Moro, *Neuropsychologia*, 2022, **174**, 108333.
- 980 8. C.-l. a. R. Labs, D. Sussillo, P. Kaifosh and T. Reardon, *Biorxiv*, 2024,
 981 2024.2002.2023.581779.
- 982 9. H. Zhang, D. Zhang, Z. Wang, G. Xi, R. Mao, Y. Ma, D. Wang, M. Tang, Z.
 983 Xu and H. Luan, *ACS Appl. Mater. Interfaces*, 2023, **15**, 5128-5138.
- 984 10. J. W. Kam, T. Rahnuma, Y. Park and C. Hart, *Neuroimage*, 2022, **258**, 119372.
- 985 11. M. Zhu, H. Wang, S. Li, X. Liang, M. Zhang, X. Dai and Y. Zhang, *Adv.
 986 Healthcare Mater.*, 2021, **10**, 2100646.
- 987 12. Y. Luo, W. Li, Q. Lin, F. Zhang, K. He, D. Yang, X. J. Loh and X. Chen, *Adv.
 988 Mater.*, 2021, **33**, 2007848.
- 989 13. P. Kateb, J. Fan, J. Kim, X. Zhou, G. A. Lodygensky and F. Cicoira, *Flexible
 990 Printed Electron.*, 2023, **8**, 045006.



- 991 14. J. Kim, J. Fan, G. Petrossian, X. Zhou, P. Kateb, N. Gagnon-Lafrenais and F. Cicoira, *Mater. Horiz.*, 2024, **11**, 3548-3560.
- 992
- 993 15. X. Zhou, P. Kateb, J. Fan, J. Kim, G. A. Lodygensky, B. Amilhon, D. Pasini and F. Cicoira, *J. Mater. Chem. C*, 2024, **12**, 5708-5717.
- 994
- 995 16. F. Han, X. Huang and E. Teye, *J. Food Process Eng.*, 2019, **42**, e12983.
- 996 17. Q. Ouyang, Y. Yang, J. Wu, Q. Chen, Z. Guo and H. Li, *Lwt*, 2020, **118**, 108768.
- 997 18. W. Zhang, C. Liu, F. Liu, X. Zou, Y. Xu and X. Xu, *Food Chem.*, 2020, **303**, 125378.
- 998
- 999 19. B. Lu, F. Han, J. H. Aheto, M. M. Rashed and Z. Pan, *Food Science & Nutrition*, 2021, **9**, 5220-5228.
- 1000
- 1001 20. H. Yin, X. Hu, X. Huang, X. Zou, Y. Xu, J. Shi and M. Yang, *Food Anal. Methods*, 2021, **14**, 1836-1842.
- 1002
- 1003 21. S. Yang and X. Jiang, *ACS Nano*, 2024, **18**, 27107-27125.
- 1004 22. H. Ullah, M. A. Wahab, G. Will, M. R. Karim, T. Pan, M. Gao, D. Lai, Y. Lin and M. H. Miraz, *Biosensors*, 2022, **12**, 630.
- 1005
- 1006 23. J. Yi, Y. Gu, J. Yang, Z. Wang, Y. Wang, W. Yan, Q. Sun, P. Zhou, Y. Xu, X. He, J. Zhong and Y. Wang, *Mater. Horiz.*, 2025, DOI: 10.1039/D4MH01858C.
- 1007
- 1008 24. J. Yang, Q. Sun, Z. Wang, Y. Xu, Y. Wang, W. Yan, P. Zhou, Z. Ji, H. Jiang, S. Chen, W. Zhang, H. Haick and Y. Wang, *Wearable Electronics*, 2025, **2**, 55-61.
- 1009
- 1010
- 1011 25. H. Wu, G. Yang, K. Zhu, S. Liu, W. Guo, Z. Jiang and Z. Li, *Adv. Sci.*, 2021, **8**, 2001938.
- 1012
- 1013 26. L. Hu, P. L. Chee, S. Sugiarto, Y. Yu, C. Shi, R. Yan, Z. Yao, X. Shi, J. Zhi and D. Kai, *Adv. Mater.*, 2023, **35**, 2205326.
- 1014
- 1015 27. L. Wang, T. Xu and X. Zhang, *TrAC Trends Anal. Chem.*, 2021, **134**, 116130.
- 1016 28. M. L. Oyen, *Int. Mater. Rev.*, 2014, **59**, 44-59.
- 1017 29. E. M. Ahmed, *J. Adv. Res.*, 2015, **6**, 105-121.
- 1018 30. H. Yuk, B. Lu and X. Zhao, *Chem. Soc. Rev.*, 2019, **48**, 1642-1667.
- 1019 31. Y. Zhao, X. Fu, B. Liu, J. Sun, Z. Zhuang, P. Yang, J. Zhong and K. Liu, *Sci. China. Mater.*, 2023, **66**, 1934-1940.
- 1020
- 1021 32. F. Mo, P. Zhou, S. Lin, J. Zhong and Y. Wang, *Adv. Healthcare Mater.*, 2024, **13**, 2401503.
- 1022
- 1023 33. Y. Huang, M. Xiao, X. Zhou, J. Zhu, Y. Tian, S. Xie, Y. Gong and J. Zhong, *Sens. Actuators B Chem.*, 2025, **431**, 137461.
- 1024
- 1025 34. Y. Liu, L. Han, S. Lv, T. Jiang, M. Duan, H. Guo, Y. Li, Q. Xie, Y. Chen and D. Wang, *Research*, 2025, **8**, 0714.
- 1026
- 1027 35. Y. Zhou, Y. Zhao, D. Zhao, X. Guan, K. Zhang, Y. Pi and J. Zhong, *Microsyst. Nanoeng.*, 2025, **11**, 40.
- 1028
- 1029 36. K. Deligkaris, T. S. Tadele, W. Olthuis and A. van den Berg, *Sens. Actuators B Chem.*, 2010, **147**, 765-774.
- 1030
- 1031 37. Y. S. Zhang and A. Khademhosseini, *Science*, 2017, **356**, eaaf3627.
- 1032 38. P. Zhou, F. Mo, Z. Ji, J. Yang, H. Du, Z. Wang, H. Haick and Y. Wang, *Sci.*



- 1033 *Bull.*, 2025, DOI: <https://doi.org/10.1016/j.scib.2025.01.058>.
- 1034 39. F. Mo, P. Zhou, S. Lin, J. Zhong and Y. Wang, *Adv. Healthcare Mater.*, 2024,
1035 **13**, 2401503.
- 1036 40. P. Zhou, Z. Zhang, F. Mo and Y. Wang, *Adv. Sens. Res.*, 2024, **3**, 2300021.
- 1037 41. F. Mo, Y. Lin, Y. Liu, P. Zhou, J. Yang, Z. Ji and Y. Wang, *Mater. Sci. Eng. R*
1038 *Rep.*, 2025, **165**, 100989.
- 1039 42. M. Niu, K. Chen, W. Li, J. Hu, J. Zhang, P. Zhu, Z. Pan and Y. Mao, *J. Mater.*
1040 *Res.*, 2024, **39**, 188-211.
- 1041 43. H. Duan, Y. Zhang, Y. Zhang, P. Zhu and Y. Mao, *Nanomaterials*, 2024, **14**,
1042 1398.
- 1043 44. W. Hu, D. Song, X. Shi and N. Liu, *SCIENTIA SINICA Chimica*, 2022, **52**, 837-
1044 847.
- 1045 45. H. Ding, Y. Gu, Y. Ren, C. Hu, Q. Qiu, D. Wu, J. Mou, Z. Wu and H. Zhou, *J.*
1046 *Mater. Chem. C*, 2024.
- 1047 46. Q. Han, C. Zhang, T. Guo, Y. Tian, W. Song, J. Lei, Q. Li, A. Wang, M. Zhang,
1048 S. Bai and X. Yan, *Adv. Mater.*, 2023, **35**, 2209606.
- 1049 47. Q. Han, X. Gao, C. Zhang, Y. Tian, S. Liang, X. Li, Y. Jing, M. Zhang, A. Wang
1050 and S. Bai, *Adv. Mater.*, 2025, **37**, 2415445.
- 1051 48. Y. Li, Y. Gu, S. Qian, S. Zheng, Y. Pang, L. Wang, B. Liu, S. Liu and Q. Zhao,
1052 *Nano Res.*, 2024, **17**, 5479-5490.
- 1053 49. Z. Zhang, J. Yang, H. Wang, C. Wang, Y. Gu, Y. Xu, S. Lee, T. Yokota, H.
1054 Haick, T. Someya and Y. Wang, *Sci. Adv.*, 2024, **10**, eadj5389.
- 1055 50. T.-C. Ho, C.-C. Chang, H.-P. Chan, T.-W. Chung, C.-W. Shu, K.-P. Chuang,
1056 T.-H. Duh, M.-H. Yang and Y.-C. Tyan, *Molecules*, 2022, **27**, 2902.
- 1057 51. T. Zhu, Y. Ni, G. M. Biesold, Y. Cheng, M. Ge, H. Li, J. Huang, Z. Lin and Y.
1058 Lai, *Chem. Soc. Rev.*, 2023, **52**, 473-509.
- 1059 52. H. Dechiraju, M. Jia, L. Luo and M. Rolandi, *Adv. Sustain. Syst.*, 2022, **6**,
1060 2100173.
- 1061 53. S. Chen, Y. Chen, X. Mu, P. Wang, L. Miao, S. Tanemura and H. Cai, *Sustain.*
1062 *Mater. Technol.*, 2023, **36**, e00635.
- 1063 54. X. Li, Y. Sun, S. Wang, G. Tian, T. Yang, L. Huang, Y. Ao, B. Lan, J. Zhang,
1064 T. Xu, Y. Liu, L. Jin, W. Yang and W. Deng, *Chem. Eng. J.*, 2024, **498**, 155195.
- 1065 55. C. G. Wang, N. E. B. Surat'man, J. J. Chang, Z. L. Ong, B. Li, X. Fan, X. J. Loh
1066 and Z. Li, *Chemistry–An Asian Journal*, 2022, **17**, e202200604.
- 1067 56. A. S. Ivanov, L. V. Pershina, K. G. Nikolaev and E. V. Skorb, *Macromol.*
1068 *Biosci.*, 2021, **21**, 2100117.
- 1069 57. D. Lu, Z. Zhu, M. Zhu, P. Zhang and X. Xiang, *J. Mater. Chem. A*, 2025, **13**,
1070 427-440.
- 1071 58. Y. Gao, W. Zhang, L. Li, Z. Wang, Y. Shu and J. Wang, *Chem. Eng. J.*, 2023,
1072 **452**, 139248.
- 1073 59. Z. Luo, W. Li, J. Yan and J. Sun, *Adv. Funct. Mater.*, 2022, **32**, 2203988.
- 1074 60. Y. Zhao, F. Wang, J. Liu, D. Gan, B. Lei, J. Shao, W. Wang, Q. Wang and X.



- 1075 Dong, *ACS Appl. Mater. Interfaces*, 2023, **15**, 28664-28674.
- 1076 61. Q. He, Y. Cheng, Y. Deng, F. Wen, Y. Lai and H. Li, *Adv. Funct. Mater.*, 2024,
- 1077 **34**, 2308974.
- 1078 62. F. Miguel, F. Barbosa, F. C. Ferreira and J. C. Silva, *Gels*, 2022, **8**, 710.
- 1079 63. M. A. Bhat, R. A. Rather and A. H. Shalla, *Synth. Met.*, 2021, **273**, 116709.
- 1080 64. B. Zhao, Z. Li, L. Zheng, Z. Ye, Y. Yuan, S. Zhang, B. Liang and T. Li, *Chin.*
- 1081 *Chem. Lett.*, 2024, **35**, 109810.
- 1082 65. R. Eivazzadeh-Keihan, E. B. Noruzi, E. Chidar, M. Jafari, F. Davoodi, A.
- 1083 Kashtiaray, M. G. Gorab, S. M. Hashemi, S. Javanshir and R. A. Cohan, *Chem.*
- 1084 *Eng. J.*, 2022, **442**, 136183.
- 1085 66. R. Arambula-Maldonado and K. Mequanint, *Materials Advances*, 2022, **3**,
- 1086 5186-5206.
- 1087 67. Y. Zhao, K. Zhao, R. Qian, Z. Yu and C. Ye, *Chem. Eng. J.*, 2024, 150197.
- 1088 68. Y. Wang, M. Zhang, Z. Yan, S. Ji, S. Xiao and J. Gao, *Theranostics*, 2024, **14**,
- 1089 1534.
- 1090 69. X. Huang, C. Chen, X. Ma, T. Zhu, W. Ma, Q. Jin, R. Du, Y. Cai, M. Zhang, D.
- 1091 Kong, M. Wang, J. a. Ren, Q. Zhang and X. Jia, *Adv. Funct. Mater.*, 2023, **33**,
- 1092 2302846.
- 1093 70. J. Dai, D. Ren, S. Zhang, Y. Liu, Y. Xiao, Z. Wang, B. Wang and F. Huang,
- 1094 *ACS Appl. Electron. Mater.*, 2025, **7**, 3125-3134.
- 1095 71. Y. Ohm, C. Pan, M. J. Ford, X. Huang, J. Liao and C. Majidi, *Nat. Electron.*,
- 1096 2021, **4**, 185-192.
- 1097 72. J. Chen, F. Liu, T. Abdiryim and X. Liu, *Adv. Compos. Hybrid Mater.*, 2024, **7**,
- 1098 35.
- 1099 73. J. Luo, C. Sun, B. Chang, Y. Jing, K. Li, Y. Li, Q. Zhang, H. Wang and C. Hou,
- 1100 *ACS Nano*, 2022, **16**, 19373-19384.
- 1101 74. C. Yu, Z. Yue, H. Zhang, M. Shi, M. Yao, Q. Yu, M. Liu, B. Guo, H. Zhang, L.
- 1102 Tian, H. Sun, F. Yao and J. Li, *Adv. Funct. Mater.*, 2023, **33**, 2211023.
- 1103 75. P. Wang, Y. Lv, J. Duan, G. Sun, C. Meng, Y. Li, S. Guo and T. Zhang, *Nano*
- 1104 *Energy*, 2025, **136**, 110722.
- 1105 76. F. Wang, L. Yang, Y. Sun, Y. Cai, X. Xu, Z. Liu, Q. Liu, H. Zhao, C. Ma and
- 1106 J. Liu, *Gels*, 2023, **9**, 323.
- 1107 77. Z. Wang, L. Chen, Y. Chen, P. Liu, H. Duan and P. Cheng, *Research*, 2020,
- 1108 **2020**.
- 1109 78. Y. Liu, C. Wang, J. Xue, G. Huang, S. Zheng, K. Zhao, J. Huang, Y. Wang, Y.
- 1110 Zhang and T. Yin, *Adv. Healthcare Mater.*, 2022, **11**, 2270092.
- 1111 79. L. Rong, X. Xie, W. Yuan and Y. Fu, *ACS Appl. Mater. Interfaces*, 2022, **14**,
- 1112 29273-29283.
- 1113 80. Y. Shi, Y. Ding, W. Wang and D. Yu, *Colloids and Surfaces A:*
- 1114 *Physicochemical and Engineering Aspects*, 2023, **675**, 132081.
- 1115 81. R. Liu, T. Wang, G. Li, Z. Fan, Q. Zhou, K. Wang, P. Li and W. Huang, *Adv.*
- 1116 *Funct. Mater.*, 2023, **33**, 2214917.



- 1117 82. Q. Liang, X. Xia, X. Sun, D. Yu, X. Huang, G. Han, S. M. Mugo, W. Chen and
1118 Q. Zhang, *Adv. Sci.*, 2022, **9**, 2201059.
- 1119 83. Q. Wu, A. Chen, Y. Xu, S. Han, J. Zhang, Y. Chen, J. Hang, X. Yang and L.
1120 Guan, *Soft Matter*, 2024, **20**, 3666-3675.
- 1121 84. X. Pan, Q. Wang, P. He, K. Liu, Y. Ni, X. Ouyang, L. Chen, L. Huang, H. Wang
1122 and Y. Tan, *ACS Sustain. Chem. Eng.*, 2019, **7**, 7918-7925.
- 1123 85. M. Lu, L. Shen, H. Su, B. Li, L. Wang and W. W. Yu, *J. Colloid Interface Sci.*,
1124 2025, **684**, 272-282.
- 1125 86. H. Ma, J. Hou, X. Xiao, R. Wan, G. Ge, W. Zheng, C. Chen, J. Cao, J. Wang,
1126 C. Liu, Q. Zhao, Z. Zhang, P. Jiang, S. Chen, W. Xiong, J. Xu and B. Lu, *J.*
1127 *Colloid Interface Sci.*, 2024, **654**, 639-648.
- 1128 87. J. Lao, Y. Jiao, Y. Zhang, H. Xu, Y. Wang, Y. Ma, X. Feng and J. Yu, *ACS*
1129 *Nano*, 2025, **19**, 7755-7766.
- 1130 88. J. Zheng, J. Zhou, Y. Zhao, C. Wang, M. Fan, Y. Li, C. Yang and H. Yang,
1131 *Biosensors*, 2025, **15**, 177.
- 1132 89. X. Xia, Q. Liang, X. Sun, D. Yu, X. Huang, S. M. Mugo, W. Chen, D. Wang
1133 and Q. Zhang, *Adv. Funct. Mater.*, 2022, **32**, 2208024.
- 1134 90. H. Xue, D. Wang, M. Jin, H. Gao, X. Wang, L. Xia, D. a. Li, K. Sun, H. Wang,
1135 X. Dong, C. Zhang, F. Cong and J. Lin, *Microsyst. Nanoeng.*, 2023, **9**, 79.
- 1136 91. N. Li, X. Wang, Y. Liu, Y. Li, J. Li, Z. Qin and T. Jiao, *Chem. Eng. J.*, 2024,
1137 **483**, 149303.
- 1138 92. J. Wei, H. Chen, F. Pan, H. Zhang, K. Yang, T. Yuan, Y. Fang, H. Ping, Q.
1139 Wang and Z. Fu, *ACS Nano*, 2025, **19**, 15554-15564.
- 1140 93. X. Zhou, A. Rajeev, A. Subramanian, Y. Li, N. Rossetti, G. Natale, G. A.
1141 Lodygensky and F. Cicoira, *Acta Biomater.*, 2022, **139**, 296-306.
- 1142 94. H. Huang, J. Shen, S. Wan, L. Han, G. Dou and L. Sun, *ACS Appl. Mater.*
1143 *Interfaces*, 2023, **15**, 11549-11562.
- 1144 95. D. Kim, H. J. Lee, J. Oh, H. Y. Yang, H. J. Park, C. Huh, D. H. Ha, Y. Jun and
1145 Y. J. Yun, *J. Mater. Chem. C*, 2025, **13**, 5711-5718.
- 1146 96. M. Li, W. Li, Q. Guan, J. Lv, Z. Wang, L. Ding, C. Li, E. Saiz and X. Hou,
1147 *Device*, 2023, **1**.
- 1148 97. H. Su, L. Mao, X. Chen, P. Liu, J. Pu, Z. Mao, T. Fujiwara, Y. Ma, X. Mao and
1149 T. Li, *Adv. Sci.*, 2024, **11**, 2405273.
- 1150 98. B. Yao, Y. Yan, Q. Cui, S. Duan, C. Wang, Y. Du, Y. Zhao, D. Wu, S. Wu, X.
1151 Zhu, T. Hsiai and X. He, *Matter*, 2022, **5**, 4407-4424.
- 1152 99. C. Liu, Y. Wang, S. Shi, Y. Zheng, Z. Ye, J. Liao, Q. Sun, B. Dang and X. Shen,
1153 *ACS Nano*, 2024, **18**, 27420-27432.
- 1154 100. H. He, H. Li, A. Pu, W. Li, K. Ban and L. Xu, *Nat. Commun.*, 2023, **14**, 759.
- 1155 101. J. Zhang, Y. Wang, Q. Wei, Y. Wang, M. Lei, M. Li, D. Li, L. Zhang and Y.
1156 Wu, *Gels*, 2021, **7**, 216.
- 1157 102. Z. Chen, Y. Chen, M. S. Hedenqvist, C. Chen, C. Cai, H. Li, H. Liu and J. Fu,
1158 *J. Mater. Chem. B*, 2021, **9**, 2561-2583.



- 1159 103. W. Li, J. Liu, J. Wei, Z. Yang, C. Ren and B. Li, *Adv. Funct. Mater.*, 2023, **33**, 2213485. View Article Online
DOI: 10.1039/D3TC01896J
- 1160
- 1161 104. J. Zhang, Y. Hu, L. Zhang, J. Zhou and A. Lu, *Nano-Micro Lett.*, 2022, **15**, 8.
- 1162 105. G. Kougkolos, M. Golzio, L. Laudebat, Z. Valdez-Nava and E. Flahaut, *J.*
- 1163 *Mater. Chem. B*, 2023, **11**, 2036-2062.
- 1164 106. L. Li, J. Meng, M. Zhang, T. Liu and C. Zhang, *Chem. Commun. (Cambridge,*
- 1165 *U. K.)*, 2022, **58**, 185-207.
- 1166 107. Z. Wang, X. Xu, R. Tan, S. Zhang, K. Zhang and J. Hu, *Adv. Funct. Mater.*,
- 1167 2024, **34**, 2312667.
- 1168 108. Q. Zhang, H. Lu, G. Yun, L. Gong, Z. Chen, S. Jin, H. Du, Z. Jiang and W. Li,
- 1169 *Adv. Funct. Mater.*, 2024, **34**, 2308113.
- 1170 109. S. Li, Y. Cong and J. Fu, *J. Mater. Chem. B*, 2021, **9**, 4423-4443.
- 1171 110. X. Ma, X. Zhou, J. Ding, B. Huang, P. Wang, Y. Zhao, Q. Mu, S. Zhang, C.
- 1172 Ren and W. Xu, *J. Mater. Chem. A*, 2022, **10**, 11823-11853.
- 1173 111. X. Shi and P. Wu, *Small*, 2021, **17**, 2101220.
- 1174 112. X. Shi and P. Wu, *Small*, 2021, **17**, 2101220.
- 1175 113. Y. Gao, K. Wu and Z. Suo, *Adv. Mater.*, 2019, **31**, 1806948.
- 1176 114. T. Wang, P. Zhang, X. Yang, Y. Zhang, J. Zhang, X. He, P. Gu, X. Gong and
- 1177 Y. Zhao, *Chem. Eng. J.*, 2022, **438**, 135441.
- 1178 115. Z. Xu, X. Liang, W. Ma, X. An, H. Wu, Q. Zhang and X. Jia, *Adv. Funct. Mater.*,
- 1179 2024, **34**, 2310233.
- 1180 116. Y. Liu, P. Wang, X. Su, L. Xu, Z. Tian, H. Wang, G. Ji and J. Huang, *Adv.*
- 1181 *Mater.*, 2022, **34**, 2108820.
- 1182 117. G. Bovone, O. Y. Dudaryeva, B. Marco-Dufort and M. W. Tibbitt, *ACS*
- 1183 *Biomater. Sci. Eng.*, 2021, **7**, 4048-4076.
- 1184 118. Y. Zhao, S. Song, X. Ren, J. Zhang, Q. Lin and Y. Zhao, *Chem. Rev.*, 2022,
- 1185 **122**, 5604-5640.
- 1186 119. Y.-W. Lee, S. Chun, D. Son, X. Hu, M. Schneider and M. Sitti, *Adv. Mater.*,
- 1187 2022, **34**, 2109325.
- 1188 120. L. Nicolle, C. M. Journot and S. Gerber-Lemaire, *Polymers*, 2021, **13**, 4118.
- 1189 121. W. Zhang, Y. Zhang, Y. Zhang, Y. Dai, F. Xia and X. Zhang, *J. Mater. Chem.*
- 1190 *B*, 2021, **9**, 5954-5966.
- 1191 122. X. Wei, Y. Wang, Y. Liu, K. Ji, K. Li, J. Wang and Z. Gu, *Matter*, 2024, **7**, 826-
- 1192 854.
- 1193 123. S. Jia, T. Tao, J. Sun, J. Du, Y. Xie, L. Yu, W. Tang, J. Wang and J. Gong,
- 1194 *Small Structures*, 2023, **4**, 2300139.
- 1195 124. G. Giordano, M. Carlotti and B. Mazzolai, *Adv. Mater. Technol.*, 2021, **6**,
- 1196 2100437.
- 1197 125. T. Cheng, Y. Z. Zhang, S. Wang, Y. L. Chen, S. Y. Gao, F. Wang, W. Y. Lai
- 1198 and W. Huang, *Adv. Funct. Mater.*, 2021, **31**, 2101303.
- 1199 126. Y. Zhang, X. Sun, Y. Ye, H. Oguzlu, Y. Zhu, J. Zhu, K. Le, P. Yang and F.
- 1200 Jiang, *Mater. Today*, 2024, **74**, 67-76.



- 1201 127. W. Li, S. Zheng, X. Zou, Y. Ren, Z. Liu, W. Peng, X. Wang, D. Liu, Z. Shen, Y. Hu, J. Guo, Z. Sun and F. Yan, *Adv. Funct. Mater.*, 2022, **32**, 2207348. View Article Online
DOI: 10.1039/D5TC01896J
- 1202
- 1203 128. R. Ji, S. Yan, Z. Zhu, Y. Wang, D. He, K. Wang, D. Zhou, Q. Jia, X. Wang, B. Zhang, C. Shi, T. Xu, R. Wang, R. Wang and Y. Zhou, *Adv. Sci.*, 2024, **11**, 2401869.
- 1204
- 1205
- 1206 129. J. Yang, Z. Zhang, P. Zhou, Y. Zhang, Y. Liu, Y. Xu, Y. Gu, S. Qin, H. Haick and Y. Wang, *Nanoscale*, 2023, **15**, 3051-3078.
- 1207
- 1208 130. Y. Wang, *Soft Sci*, 2024, **4**.
- 1209 131. Y. Wang, H. Haick, S. Guo, C. Wang, S. Lee, T. Yokota and T. Someya, *Chem. Soc. Rev.*, 2022, **51**, 3759-3793.
- 1210
- 1211 132. S. Cheng, Z. Lou, L. Zhang, H. Guo, Z. Wang, C. Guo, K. Fukuda, S. Ma, G. Wang, T. Someya, H.-M. Cheng and X. Xu, *Adv. Mater.*, 2023, **35**, 2206793.
- 1212
- 1213 133. S. Wei, R. Yin, T. Tang, Y. Wu, Y. Liu, P. Wang, K. Wang, M. Mei, R. Zou and X. Duan, *ACS Nano*, 2019, **13**, 7920-7929.
- 1214
- 1215 134. B. Khan, Z. Riaz and B. L. Khoo, *Mater. Sci. Eng. R Rep.*, 2024, **159**, 100804.
- 1216 135. P. A. Moreno-Sánchez, G. García-Isla, V. D. Corino, A. Vehkaoja, K. Brukamp, M. Van Gils and L. Mainardi, *Comput. Biol. Med.*, 2024, 108235.
- 1217
- 1218 136. J. C. Hwang, M. Kim, S. Kim, H. Seo, S. An, E. H. Jang, S. Y. Han, M. J. Kim, N. K. Kim and S.-W. Cho, *Sci. Adv.*, 2022, **8**, eabq0897.
- 1219
- 1220 137. S.-H. Sunwoo, S. I. Han, C. S. Park, J. H. Kim, J. S. Georgiou, S.-P. Lee, D.-H. Kim and T. Hyeon, *Nat. Rev. Bioeng.*, 2024, **2**, 8-24.
- 1221
- 1222 138. B. Pan, F. Xiong, J. Wang, J. Fu, Y. Ding, R. Qin and S. Li, *Talanta*, 2025, 127591.
- 1223
- 1224 139. Y. Du, J. H. Kim, H. Kong, A. A. Li, M. L. Jin, D. H. Kim and Y. Wang, *Adv. Healthcare Mater.*, 2024, **13**, 2303461.
- 1225
- 1226 140. S. Tang, D. Sha, Z. He, X. Chen, Y. Ma, C. Liu and Y. Yuan, *Adv. Healthcare Mater.*, 2023, **12**, 2300475.
- 1227
- 1228 141. Y. Zhang, Q. Tang, J. Zhou, C. Zhao, J. Li and H. Wang, *ACS Biomater. Sci. Eng.*, 2023, **10**, 191-218.
- 1229
- 1230 142. X. Shi, H. Yu, Z. Tang, S. Lu, M. You, H. Yin and Q. Chen, *Sci. China Technol. Sci.*, 2024, **67**, 3136-3151.
- 1231
- 1232 143. G. Yang, Z. Lan, H. Gong, J. Wen, B. Pang, Y. Qiu, Y. Zhang, W. Guo, T. Bu, B. Xie and H. Wu, *Adv. Funct. Mater.*, 2025, **35**, 2417841.
- 1233
- 1234 144. S. Chen, Q. Ouyang, X. Meng, Y. Yang, C. Li, X. Miao, Z. Chen, G. Zhao, Y. Lei, B. Ghanem, S. Gautam, J. Cheng and Z. Yan, *Sci. Adv.*, 2025, **11**, eadv2406.
- 1235
- 1236 145. D. Farina, R. Merletti and R. M. Enoka, *J. Appl. Physiol.*, 2004, **96**, 1486-1495.
- 1237 146. H. Wang, Q. Ding, Y. Luo, Z. Wu, J. Yu, H. Chen, Y. Zhou, H. Zhang, K. Tao and X. Chen, *Adv. Mater.*, 2024, **36**, 2309868.
- 1238
- 1239 147. S. Yang, J. Cheng, J. Shang, C. Hang, J. Qi, L. Zhong, Q. Rao, L. He, C. Liu and L. Ding, *Nat. Commun.*, 2023, **14**, 6494.
- 1240
- 1241 148. J. Wu, J. Xian, C. He, H. Lin, J. Li and F. Li, *Adv. Mater.*, 2024, **36**, 2405372.
- 1242 149. Y. Zhang, L. Chen, M. Xie, Z. Zhan, D. Yang, P. Cheng, H. Duan, Q. Ge and



- 1243 Z. Wang, *Mater. Today Phys.*, 2022, **27**, 100794.
- 1244 150. J. Park, Y. Lee, S. Cho, A. Choe, J. Yeom, Y. G. Ro, J. Kim, D.-h. Kang, S. Lee
1245 and H. Ko, *Chem. Rev.*, 2024, **124**, 1464-1534.
- 1246 151. H. Yuk, J. Wu and X. Zhao, *Nature Reviews Materials*, 2022, **7**, 935-952.
- 1247 152. J.-W. Lee, M.-J. Shin, M.-H. Jang, W.-B. Jeong and S.-J. Ahn, *Med. Eng. Phys.*,
1248 2021, **98**, 65-72.
- 1249 153. V. Alcan and M. Zinnuroğlu, *Turkish journal of medical sciences*, 2023, **53**,
1250 1019-1031.
- 1251 154. Q. Liu, X. Xu, Y. Zhang, L. Liang, B. Zhang and S. Chen, *Chem. Eng. J.*, 2025,
1252 **509**, 161207.
- 1253 155. S. Roubert Martinez, P. Le Floch, J. Liu and R. D. Howe, *Adv. Healthcare*
1254 *Mater.*, 2023, **12**, 2202661.
- 1255 156. R. Wan, J. Yu, Z. Quan, H. Ma, J. Li, F. Tian, W. Wang, Y. Sun, J. Liu and D.
1256 Gao, *Chem. Eng. J.*, 2024, **490**, 151454.
- 1257 157. R. Wan, S. Liu, Z. Li, G. Li, H. Li, J. Li, J. Xu and X. Liu, *J. Colloid Interface*
1258 *Sci.*, 2025, **677**, 198-207.
- 1259 158. T. Li, H. Qi, C. Zhao, Z. Li, W. Zhou, G. Li, H. Zhuo and W. Zhai, *Nat.*
1260 *Commun.*, 2025, **16**, 88.
- 1261 159. J. Gavvala, N. Abend, S. LaRoche, C. Hahn, S. T. Herman, J. Claassen, M.
1262 Macken, S. Schuele, E. Gerard and C. C. E. M. R. Consortium, *Epilepsia*, 2014,
1263 **55**, 1864-1871.
- 1264 160. C. De Gans, P. Burger, E. Van den Ende, J. Hermanides, P. Nanayakkara, R.
1265 Gemke, F. Rutters and D. Stenvers, *Sleep Med. Rev.*, 2024, 101951.
- 1266 161. M. Mohamed, N. Mohamed and J. G. Kim, *Biosensors*, 2023, **13**, 1019.
- 1267 162. J.-C. Hsieh, W. He, D. Venkatraghavan, V. B. Koptelova, Z. J. Ahmad, I.
1268 Pyatnitskiy, W. Wang, J. Jeong, K. K. W. Tang and C. Harmeier, *Device*, 2024,
1269 **2**.
- 1270 163. X. Li, Y. Zhang, P. Tiwari, D. Song, B. Hu, M. Yang, Z. Zhao, N. Kumar and
1271 P. Marttinen, *ACM Computing Surveys*, 2022, **55**, 1-57.
- 1272 164. G. Yang, K. Zhu, W. Guo, D. Wu, X. Quan, X. Huang, S. Liu, Y. Li, H. Fang
1273 and Y. Qiu, *Adv. Funct. Mater.*, 2022, **32**, 2200457.
- 1274 165. M. Hu, J. Ren, Y. Pan, L. Cheng, X. Xu, C. L. Tan, H. Sun, Y. Shi and S. Yan,
1275 *Adv. Funct. Mater.*, 2024, **34**, 2407926.
- 1276 166. G. Li, Y. Liu, Y. Chen, M. Li, J. Song, K. Li, Y. Zhang, L. Hu, X. Qi and X.
1277 Wan, *J. Neural Eng.*, 2023, **20**, 026017.
- 1278 167. J. Liu, S. Lin, W. Li, Y. Zhao, D. Liu, Z. He, D. Wang, M. Lei, B. Hong and H.
1279 Wu, *Research*, 2022.
- 1280 168. W. U. Khan, Z. Shen, S. M. Mugo, H. Wang and Q. Zhang, *Chem. Soc. Rev.*,
1281 2025, **54**, 2832-2880.
- 1282 169. Q. Han, C. Zhang, T. Guo, Y. Tian, W. Song, J. Lei, Q. Li, A. Wang, M. Zhang
1283 and S. Bai, *Adv. Mater.*, 2023, **35**, 2209606.
- 1284 170. C. Wang, H. Wang, B. Wang, H. Miyata, Y. Wang, M. O. G. Nayeem, J. J. Kim,



- 1285 S. Lee, T. Yokota, H. Onodera and T. Someya, *Sci. Adv.*, 2022, **8**, eabo1396. [View Article Online](#)
 1286 171. L. Li, X. Ye, Z. Ji, M. Zheng, S. Lin, M. Wang, J. Yang, P. Zhou, Z. Zhang, B.
 1287 Wang, H. Wang and Y. Wang, *Small*, 2025, **21**, 2407996. DOI: 10.1039/D5TC01896J
 1288 172. G. Fang, X. Yang, Q. Wang, A. Zhang and B. Tang, *Materials Science and*
 1289 *Engineering: C*, 2021, **127**, 112212.
 1290 173. R. Lev and D. Seliktar, *J. Royal Soc. Interface*, 2018, **15**, 20170380.
 1291 174. N. A. Alba, R. J. Sclabassi, M. Sun and X. T. Cui, *IEEE Trans. Neural Syst.*
 1292 *Rehabil. Eng.*, 2010, **18**, 415-423.
 1293 175. J. S. Blasco, E. Iáñez, A. Ubeda and J. M. Azorín, *Expert Systems with*
 1294 *Applications*, 2012, **39**, 7908-7918.
 1295 176. G. Perale, F. Rossi, E. Sundstrom, S. Bacchiega, M. Masi, G. Forloni and P.
 1296 Veglianesi, *ACS Chem. Neurosci.*, 2011, **2**, 336-345.
 1297 177. K. Pradhan, G. Das, J. Khan, V. Gupta, S. Barman, A. Adak and S. Ghosh,
 1298 *ACS Chem. Neurosci.*, 2018, **10**, 1535-1543.
 1299 178. V. Martínez-Cagigal, J. Thielen, E. Santamaria-Vazquez, S. Pérez-Velasco, P.
 1300 Desain and R. Hornero, *J. Neural Eng.*, 2021, **18**, 061002.
 1301 179. J. Sosulski and M. Tangermann, *J. Neural Eng.*, 2022, **19**, 066001.
 1302 180. M. Zheng, L. Li, X. Ye, Z. Ji, Y. Wang, Z. Wang, S. Lin, M. Wang, W. Yan, J.
 1303 Yang, P. Zhou, Y. Zhang, R. Niu, H. Haick and Y. Wang, *Chem. Eng. J.*, 2025,
 1304 **512**, 162451.
 1305 181. X. Pan, J. Guan, S. Cao, X. Ma, Y. Ni and Q. Wang, *J. Colloid Interface Sci.*,
 1306 2025, **680**, 753-761.

1307



Data availability

The data that support the findings of this study are available from the corresponding author upon reasonable request.

